Modeling and Implementation of Plates with Enhanced Active Constrained Layer Damping

by

Dai Ruoli

A Thesis Submitted in Partial Fulfillment

of the Requirements for the Degree of

Master of Philosophy

in

Automation & Computer-Aided Engineering

July 2004

ABSTRACT

An active constrained layer (ACL) damping treatment with edge elements for active-passive hybrid vibration control of a plate is considered in this study. The enhanced active constrained layer (EACL) damping treatment was first proposed by Liao and Wang [1996] to improve the actuating ability of the active constrained layer (ACL) patch. However, this treatment is only considered in one-dimensional structures such as beams. This treatment is expanded to two-dimensional plate structures in this study. Finite element method is used to model the EACL plate structure. Two dimensional rectangular plate elements are used to model the base plate and the piezoelectric constraining layer. In the EACL configuration, the edge element is modeled as equivalent shear modulus. To be formulated in time domain, the Golla-Hughes-McTavish (GHM) method instead of complex shear modulus is used to model viscoelastic materials while structural damping is given by Rayleigh damping. Partially covered cantilever plates with ACL and EACL patches are developed while their bending and torsion modes are excited to validate the FEM model. The EACL patch location is also studied with this validated model. The positive position feedback (PPF) controller is used for providing active damping. Closed loop EACL systems are implemented. The vibration performances of the ACL and EACL plate systems are analyzed and experimentally compared. The results show that the multiple modes of a plate can be effectively suppressed with one single EACL patch and PPF controllers.

摘要

本論文的研究對象是一種增加了邊端元體的主動阻尼層裝置，我們稱其為增強型主動阻尼層裝置。這種由廖維新與王光偉1996年提出以改善驅動能力的裝置被用於一維的梁結構的主被動混合振動控制當中。在本研究中，這種裝置被推廣到了兩維的板結構的振動控制當中。本研究為板結構上的增強型主動阻尼層裝置建立了有限元模型，模型中使用矩形板單元來模擬板以及阻尼層裝置，而增強型阻尼層裝置中的邊端元體使用了等效剪切彈性模量來模擬。爲了使模型能運用於時域，本模型摒棄了傳統使用的複數剪切模量，引入了能夠同時運用於頻域和時域的GHM方法來模擬阻尼層中的粘彈性材料。同時，模型使用了Rayleigh方法來模擬結構內部本身帶來的阻尼。實驗和模擬研究了板的彎曲與扭轉等不同的模態。論文中還給出了算例，對阻尼層裝置的貼片位置進行了討論，該算例對模型的應用給出了範例。本研究中使用了正位反饋控制元來提供主動控制信號。作者對貼有增強型主動阻尼層裝置的懸臂板結構進行了大量的實驗研究，對傳統主動阻尼層和增強型阻尼層裝置在板結構中的實際減振效果進行了對比。結果表明，結合正位反饋控制元的增強型主動阻尼層裝置能更加有效的對板結構的各個模態的振動進行控制。

ACKNOWLEDGEMENTS

My sincere gratitude goes to my supervisor, Professor Liao Wei-Hsin, who makes this thesis possible. I am also very grateful to Professor Yam Yeung, Professor Du Ruxu for serving as my committee members and providing comments on this research.

I would like to express my appreciation to my parents and Miss Leng Jing for their love and support over the years; SMS Lab members — Frankie, Jackie, Tom and Chris — for the discussions and their help in experiments; Shaojie, Jianjun, Mark, Wei, Yong, Ding and Sera for their friendship and additional thanks to Diablo II and the basketball games during my spare time. Finally, to all the above — thanks, with love.

TABLE OF CONTENTS

ABSTRACT i
摘要 ii
ACKNOWLEDGEMENTS iii
TABLE OF CONTENTS iv
LIST OF FIGURES vi
LIST OF TABLES ix

CHAPTER ONE – BACKGROUND AND LITERATURE REVIEW 1

1.1 Piezoelectric Materials 2
1.2 Literature Review on Vibration Control 6
1.2.1 Passive control (PCL treatment) 6
1.2.2 Active control (PA treatment) 7
1.2.3 Active passive hybrid control (ACL and EACL treatment) 8
1.3 Finite Element Method 11
1.4 Positive Position Feedback Control 12
1.5 Damping 13
1.5.1 GHM method 13
1.5.2 Rayleigh damping 13
1.6 Thesis Objectives and Outline 15

CHAPTER TWO – SYSTEM MODELING 16

2.1 Assumptions 17
2.2 Elements 18
2.3 FEM Matrices 22
2.3.1 Element matrices component related to in-plane displacement 22
2.3.2 Element matrices component related to bending displacement 30
2.3.3 Element matrices component related to shear strain 35
2.3.4 Overall element matrices 38
2.3.5 Piezoelectric control forces 39
2.4 Damping 40
2.4.1 Damping due to the viscoelastic materials 40
2.4.2 Inherent structural damping 43
2.5 Edge Elements 44
2.6 Model Reduction 46

CHAPTER THREE – MODEL VALIDATION 47

3.1 Beam with Passive ACL Damping Treatment 48
3.2 Clamped-Clamped Plate with Fully Covered ACL 50
3.3 Cantilever Plate with ACL/EACL Patch 52

CHAPTER FOUR – STUDIES ON EACL PATCH LOCATION 57

4.1 Overview of the Numerical Examples 58
4.2 Patch Location on Passive Damping Ability 61
4.3 Patch Location on Actuating Ability 65
4.4 Discussion on Patch Location 69

CHAPTER FIVE – SYSTEM IMPLEMENTATION 71

5.1 Experimental Setup 71
5.1.1 Open loop test 72
5.1.2 Closed loop test 72
5.2 Controller Design 74
5.3 Results and Discussion 76

CHAPTER SIX – CONCLUSION AND FUTURE WORK 81

6.1 Summary and Conclusion 81
6.2 Recommendations for Future Research 82

APPENDIX – PZT data sheet from PIEZO SYSTEMS, INC. 83

BIBLIOGRAPHY 85

LIST OF FIGURES

Figure 1.1.1 Vertical (d33) motor [www.piezo.com] 5

Figure 1.1.2 In-plane (d31, d32) motor [www.piezo.com] 5

Figure 1.2.1 Structure with passive constrained layer damping treatment 6

Figure 1.2.2 Structure with purely active treatment 7

Figure 1.2.3 Structure with active constrained layer treatment 8

Figure 1.2.4 Structure with enhanced active constrained layer treatment 9

Figure 1.4.1 Block diagram of a second order system with PPF controller 12

Figure 2.2.1 Coordinate system of the cantilever plate with finite elements 18

Figure 2.2.2 Undeflected cross section and deflected cross section 19

Figure 2.2.3 Finite element mesh and element types 21

Figure 2.3.1 Geometry of the rectangular element ($\xi=x/a$, $\eta=y/b$) 23

Figure 2.3.2 Geometry of a rectangular bending element ($\xi=x/a$, $\eta=y/b$) 30

Figure 2.3.3 Geometry of displacements and VEM shear strains 35

Figure 2.4.1 The mini-oscillator mechanical analogy used in the GHM method 41

Figure 3.1.1 Experimental setup for testing the passive damping of the beam with ACL 48

Figure 3.1.2 Time response of tip displacement of the beam 49

Figure 3.1.3 Frequency response of tip displacement receptance of the beam 49

Figure 3.2.1 Experimental result of Clamped-Clamped plate with ACL treatment 51

Figure 3.2.2 Simulation results for the experiment by Chantalakhana and Stanway 51

Figure 3.3.1 The first three mode shapes of the C-F plain plate 53

Figure 3.3.2 Finite element mesh of the C-F plate with single EACL patch 54

Figure 3.3.3 Open loop frequency response of the plate with ACL..... 55

Figure 3.3.4 Open loop frequency response of the plate with EACL 55

Figure 4.1.1 EACL treated plate dimension and patch location 58

Figure 4.1.2 The first six mode shapes of the cantilever plate..... 60

Figure 4.2.1 Damping ratio of the first mode versus patch location 61

Figure 4.2.2 Damping ratio of the second mode versus patch location 62

Figure 4.2.3 Damping ratio of the third mode versus patch location..... 62

Figure 4.2.4 Damping ratio of the fourth mode versus patch location..... 63

Figure 4.2.5 Damping ratio of the fifth mode versus patch location..... 63

Figure 4.3.1 Resonant amplitude of the first mode versus patch location 66

Figure 4.3.2 Resonant amplitude of the second mode versus patch location..... 66

Figure 4.3.3 Resonant amplitude of the third mode versus patch location 67

Figure 4.3.4 Resonant amplitude of the fourth mode versus patch location 67

Figure 4.3.5 Resonant amplitude of the fifth mode versus patch location..... 68

Figure 5.1.1 The cantilever plate and related equipment 71

Figure 5.1.2 The open loop experimental setup 72

Figure 5.1.3 The closed loop experiment setup..... 73

Figure 5.2.1 Overall control circuit 75

Figure 5.2.2 PPF filter 75

Figure 5.3.1 Time response of the EACL plate..... 77

Figure 5.3.2 Frequency response of the EACL plate 77

Figure 5.3.3 Frequency response of the EACL plate (2nd mode suppression)..... 78

Figure 5.3.4 Frequency response of the ACL plate..... 79

Figure 5.3.5 Time response of the EACL plate..... 80

Figure 5.3.6 Frequency response of the EACL plate 80

LIST OF TABLES

Table 2.4.1 The 3 term GHM parameters 42

Table 3.2.1 The experimental and simulation results (C-C plate with ACL) 50

Table 3.3.1 System parameters 52

Table 3.3.2 The experimental and simulation results for the plate with open loop ACL treatment 56

Table 3.3.3 The experimental and simulation results for the plate with open loop EACL treatment 56

Table 4.2.1 Patch locations for best passive damping 64

Table 4.3.1 Best actuating authority patch locations 68

Table 5.2.1 PPF filter parameters 75

Table 5.3.1 The open loop and closed loop damping ratios of EACL treated plate (first 3 modes damped) 77

Table 5.3.2 The open loop and closed loop damping ratios of the EACL treated plate (second mode suppressed) 78

CHAPTER ONE

BACKGROUND AND LITERATURE REVIEW

Vibration control is an important issue as people often experience vibration in their daily life. Structures may suffer from damage due to vibrations especially under their resonant frequencies. Therefore, structural vibration control is an essential research area.

This chapter presents preliminary knowledge and related literatures on this research subject. Firstly, some background on piezoelectric materials and a brief discussion on piezoelectric theory are given. The classification of vibration control systems is also provided. The advantages and disadvantages of those systems are discussed with a comprehensive literature review in the field of constrained layer treatments. Following is a laconic introduction to Finite Element Method (FEM), vibration and model analysis. Finally, controllers and damping modeling approaches used in this research are discussed.

1.1 Piezoelectric Materials

Piezoelectric materials generate electrical charge when mechanically stressed, and vice versa. In another word, piezoelectric materials can convert electrical energy to mechanical energy (work as actuators) and mechanical energy to electrical energy (work as sensors).

It was long time ago for humans to discover piezoelectricity and piezoelectric materials. The chronicle about piezoelectric materials can be found on 'http://www.piezo.com/' and extracted as follows:

DISCOVERY AND INSIGHTS
1880 – 1882

The first experimental demonstration of a connection between macroscopic piezoelectric phenomena and crystallographic structure was published in 1880 by Pierre and Jacques Curie. Their experiment consisted of a conclusive measurement of surface charges appearing on specially prepared crystals (tourmaline, quartz, topaz, cane sugar and Rochelle salt among them) which were subjected to mechanical stress.

A LABORATORY CURIOSITY - A MATHEMATICAL CHALLENGE
1882 – 1917

At this point in time, after only two years of interactive work within the European scientific community, the core of piezoelectric applications science was established: the identification of piezoelectric crystals on the basis of asymmetric crystal structure, the reversible exchange of electrical and mechanical energy, and the usefulness of thermodynamics in quantifying complex relationships among mechanical, thermal and electrical variables.

FIRST GENERATION APPLICATIONS WITH NATURAL CRYSTALS
1920 – 1940

The success of sonar stimulated intense development activity on all kinds of piezoelectric devices, both resonating and non-resonating.

SECOND GENERATION APPLICATIONS WITH PIEZOELECTRIC CERAMICS
1940 – 1965

During World War II, in the U.S., Japan and the Soviet Union, isolated research groups working on improved capacitor materials discovered that certain ceramic materials (prepared by sintering metallic oxide powders) exhibited dielectric constants up to 100 times higher than common cut crystals.

JAPANESE DEVELOPMENTS
1965 – 1980

In contrast to the "secrecy policy" practiced among U.S. piezoceramic manufacturers at the outset of the industry, several Japanese companies and universities formed a "competitively cooperative" association, established as the Barium Titanate Application Research Committee, in 1951. This association set an organizational precedent for successfully surmounting not only technical challenges and manufacturing hurdles, but also for defining new market areas.

SEARCH FOR HIGH VOLUME MARKETS
1980 – Present

The commercial success of the Japanese efforts has attracted the attention of industry in many other nations and spurred a new effort to develop successful piezoceramic products. If you have any doubts about this, just track the number of piezo patents granted by the U.S. Patent Office every year - there has been a phenomenal rise. Another measure of activity is the rate and origin of article publication in the piezo materials/applications area - there has been a large increase in publication rate in Russia, China and India.

The equivalent model for the piezoelectric materials was proposed by Dosch et al. [1992]. The linear piezoelectric constitutive equations are given by

$$T = c^E S + eE \tag{1.1.1}$$

$$D = eS + \varepsilon^S E \tag{1.1.2}$$

or

$$S = s^E T + dE \tag{1.1.3}$$

$$D = dT + \varepsilon^T E \tag{1.1.4}$$

where S is the mechanical strain, T is the mechanical stress, s^E is elastic compliance constant, d and e are piezoelectric constants, E is the electrical field, D is the electrical displacement, ε is the dielectric constant.

Some of the piezoelectric material constants in the above equations are written with a "superscript", which specifies either mechanical or electrical conditions as follows:

Superscript S for constant strain (mechanically clamped).

Superscript T for constant stress (mechanically free).

Superscript E for constant electrical field (short circuit).

Superscript D for constant electrical displacement (open circuit).

In this research, a piezoelectric element is used as an actuator. Rearrange equation (1.1.3)

$$\begin{aligned} T &= \frac{1}{s^E}(S - dE) \\ &= E_1(S - dE) \end{aligned} \tag{1.1.5}$$

where T is a 1×3 stress vector, d is a 3x3 tensor denotes the piezoelectric constant and E is a 1×3 vector denotes the applied electrical field. $E_1 = \frac{1}{s^E}$ is the Young's modulus of the piezoelectric material.

If subscripts are used, we obtain

$$T_j = \frac{V_a}{h_1} d_{ij} E_j \tag{1.1.6}$$

where i, j = 1, 2 and 3, which denote x, y and z directions respectively. The control voltage is applied to the piezoelectric element in the vertical direction (direction 3) and the piezo patch stretches and contracts in-plane (directions 1 and 2). In this case, the transverse actuating effect is ignored. d_{33} is used to quantify the effect when the electrical field is applied along the polarization axis (direction 3) and the mechanical strain is along the same axis (which is ignored here). d_{31} and d_{32} are used here if the electric field is in the 3 direction, but the strains are in the 1 and 2 axis (orthogonal to the polarization axis). That is, we only use the following two stresses in this research.

$$T_1 = E_1 \frac{V_a}{h_1} d_{31} \tag{1.1.7}$$

$$T_2 = E_1 \frac{V_a}{h_1} d_{32} \tag{1.1.8}$$

Figure 1.1.1 and Figure 1.1.2 show the model of the longitudinal actuator and the transverse actuator (which is used in this research).

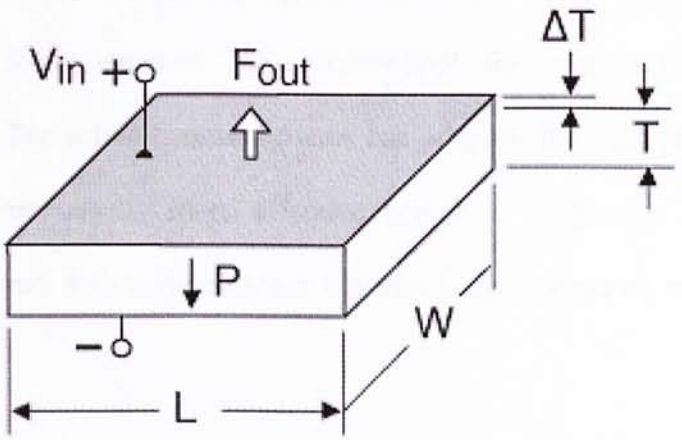

Figure 1.1.1 Vertical (d33) motor [www.piezo.com]

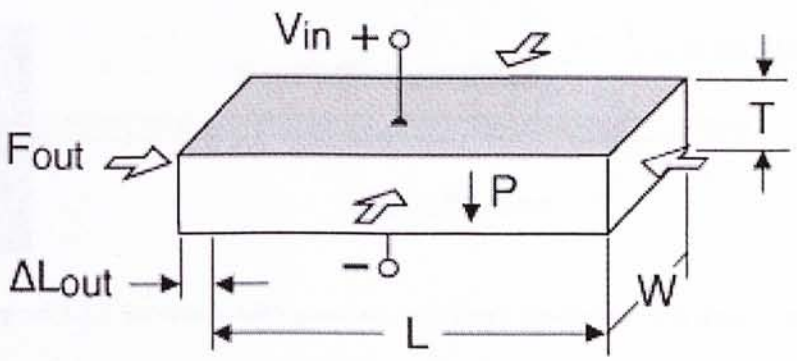

Figure 1.1.2 In-plane (d31, d32) motor [www.piezo.com]

1.2 Literature Review on Vibration Control

Typically, vibration control can be categorized into two major areas: passive and active controls. In a passive control system, no feedback action is applied to the system and the system design is fixed. Therefore, the performance may not be optimized for all operating situations. On the other hand, in an active control system, sensors are used to collect the information from the external world and the structure itself. Feeding the collected sensing signals back to a controller, the signal from the controller is then fed to actuators. The actuators apply forces or torques to the system to be controlled. The active control systems can adapt to the changes of the system parameters and are usually more effective compared to passive systems. More specific passive and active systems are discussed and compared in the following sections.

1.2.1 Passive control (PCL treatment)

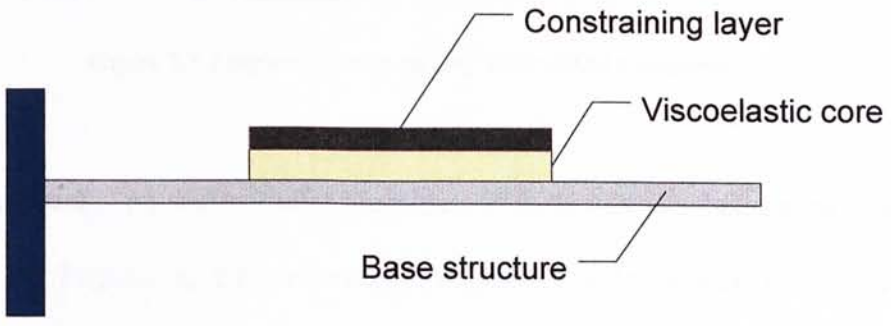

Figure 1.2.1 Structure with passive constrained layer damping treatment

The passive constrained layer (PCL) damping treatment is a typical passive control approach. As we can see in Figure 1.2.1, a constraining layer is patched on the top of

a viscoelastic layer that is stuck directly on the base structure. The vibration of this structure is suppressed by dissipating the energy in the viscoelastic core. When the structure is vibrating, an in-plane strain difference between the base structure and the constraining layer will be induced; a shear angle of the VEM is thus produced to cause the energy dissipation. The advantages of the passive systems are fail-safe, no power requirement and simple to implement. However, since this system is fixed, the system performance may not be optimal for various situations.

1.2.2 Active control (PA treatment)

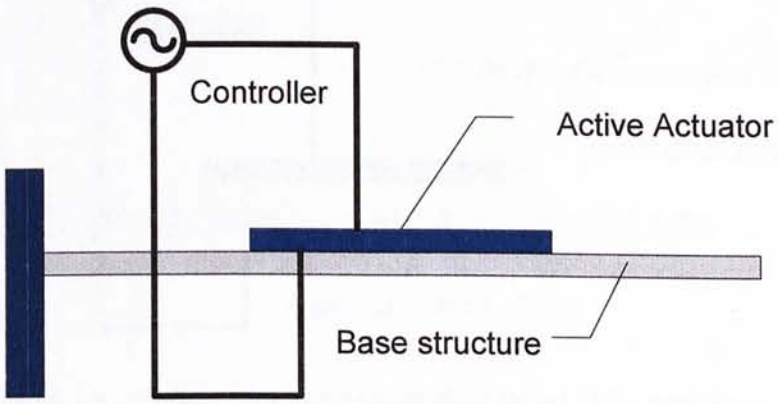

Figure 1.2.2 Structure with purely active (PA) treatment

Since 1985, researchers started to use piezoelectric materials as actuators for vibration control. At the beginning, the piezoelectric element is patched directly on the base structure, which is one kind of purely active (PA) treatment. An electrical control signal is fed to the actuator as shown in Figure 1.2.2 and the structure vibration can be suppressed by the force generated by the piezoelectric actuator. This active control system is usually more effective than the passive control system and is adaptive while

facing different conditions. However, the active control requires relatively high power supply and the system could be unstable when facing unexpected situations such as power failure. It has to be mentioned that active systems usually have poor damping performance at high frequencies. In some cases, while the active actuator is designed to suppress the lower modes of the structure, some higher modes are exited to cause the structure unstable.

1.2.3 Active passive hybrid control (ACL and EACL treatments)

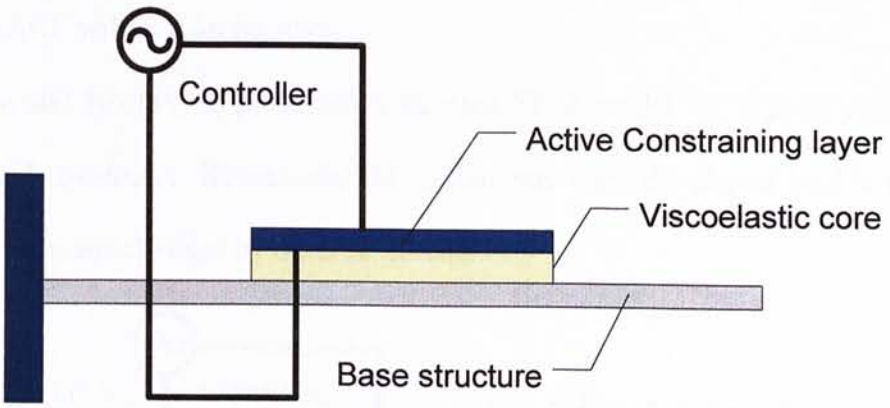

Figure 1.2.3 Structure with active constrained layer (ACL) treatment

The use of active constrained layer (ACL) damping treatments on structures was investigated by Baz and Ro [1993]. As we can see from Figure 1.2.3, in the ACL configuration, the passive and active control systems are combined. A layer of viscoelastic material (VEM) is sandwiched between the piezoelectric coversheet and the base structure. This hybrid control technique could combine the advantages of the passive and active systems. The shear angle of the VEM layer can be increased due to the controllable induced strain in the constraining layer. In this case, the energy

dissipation in the viscoelastic core will be increased due to the active control. At the same time, the VEM core ensures that the higher modes of the structure are well damped.

Baz and Ro [1994] investigated the performance characteristics of the ACL damping treatment on beam structures both analytically and experimentally before they used this treatment on a cantilever plate (Baz and Ro 1996). Shen [1996] studied the stability, controllability and observability on the ACL systems. Shen [1997] also developed an analytical model to prove the power dissipation in velocity feedback controlled ACL will remain positive.

Baz and Ro [1999] presented a detailed FEM model for a plate with fully covered ACL treatment. Rectangular ACL elements were developed in this model, which has been widely used by other researchers.

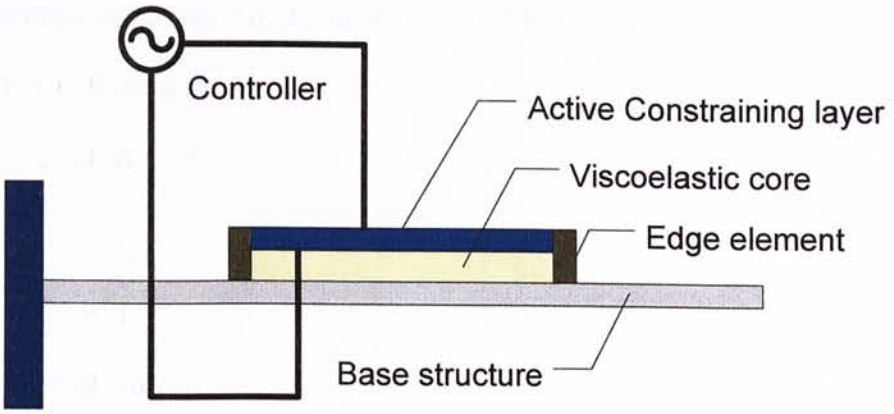

Figure 1.2.4 Structure with enhanced active constrained layer (EACL) treatment

As discussed above, the ACL treatment can increase the system damping compared with the passive system. However, Liao and Wang [1997] pointed out that the VEM layer would degrade the active control authorities. It can be easily

understood that the control force from the PZT layer will be greatly degraded while transmitting to the base structure through the soft VEM layer.

In order to overcome the negative effect of the VEM on the active action transmissibility, Liao and Wang [1996] proposed an enhanced active constrained layer (EACL) damping treatment, in which two stiff edge elements were introduced onto the boundaries of the piezoelectric actuator. It has been proved that the edge elements can effectively increase the control authorities. Liao and Wang [1998] also developed a finite element model for the EACL damping treatment for one-dimensional structures (beams). The effects of edge element stiffness on the performance of EACL were studied by Liu and Wang [1999]. They also investigated the EACL treatment for broadband damping augmentation on beam structures [2002].

This thesis will extend the previous work on the EACL treatment to two-dimensional (2D) structures, i.e., from beams to plates.

1.3 Finite Element Method

The Finite Element Method (FEM) was developed in the 1940's when the scientist came up to the problem of calculating the stresses in the aluminum skin of an aircraft wing. FEM is a powerful technique that allows us break the large geometric domain of the structure into several small subdomains (elements) and perform calculations at only a few discrete points within each element. With the use of the high speed computers, the FEM has become the most popular and user-friendly computational method used in structure design and dynamics, magnetic field computation, heat transfer, and non-linear material analysis.

The application of the finite element method to a physical problem consists of several steps. These can be listed as follows: discretization, interpolation, elemental formulation, assembly, constraints, computation and solution [Bickford, 1994]. These steps for the EACL model will be discussed in detail in subsequent chapters in this thesis.

1.4 Positive Position Feedback Control

Positive position feedback (PPF) control was firstly presented by Goh and Caughey [1985]. This control algorithm is designed for large flexible space structures. This controller is applied by feeding the structural position signal to the compensator and the control signal is produced and positively fed to the structure with the product of a control gain.

The structure and the PPF compensator are modified in time domain by

$$\begin{aligned} \psi &= \ddot{\psi}(t) + 2\xi_s \omega_s \dot{\psi}(t) + \omega_s^2 \psi(t) \\ \eta &= \ddot{\eta}(t) + 2\xi_f \omega_f \dot{\eta}(t) + \omega_f^2 \eta(t) \end{aligned} \tag{1.4.1}$$

where ψ and η are the structure and PPF filter position signal, ω_s ω_f ξ_s and ξ_f are frequencies and damping ratios of the structure and filter, respectively. Figure 1.4.1 illustrates the single degree-of-freedom (SDOF) control system with control gain K_{ppf}.

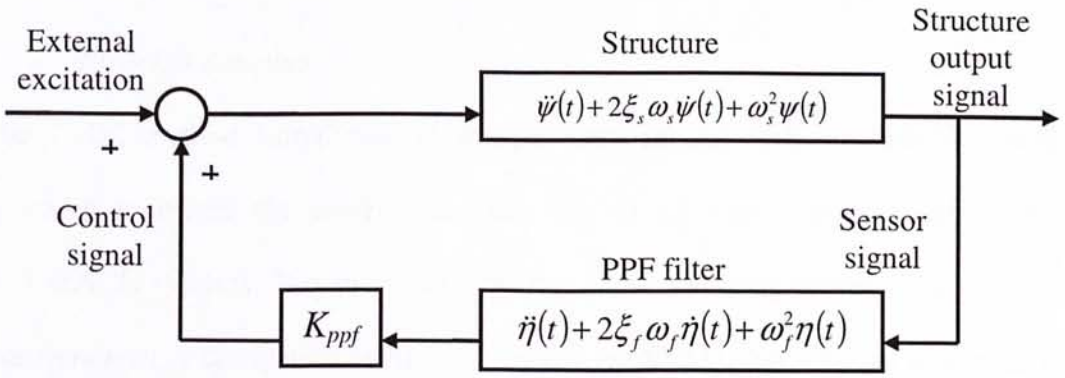

Figure 1.4.1 Block diagram of a second order system with PPF controller

1.5 Damping

In this research, the passive damping in the FEM model is modeled by the combination of the Golla-Hughes-McTavish (GHM) method and Rayleigh damping.

1.5.1 GHM method

The GHM Method was firstly presented by Golla and Hughes [1985], McTavish and Hughes [1993] to model viscoelastic materials. The GHM method models the energy dissipation in viscoelastic materials with the consideration of thermodynamic principles. It should be noted that this method can be applied in time domain.

Dissipation coordinates are introduced in this method and these new coordinates require curve fitting to loss factor data over certain range of frequencies. Lam [1995] used the GHM method to model VEM damping for the ACL treatment. Liao [1997] also applied the GHM method for the ACL and EACL systems.

The GHM parameters used in this thesis were given by Liao [1997]. The VEM used in this research (ISD112, 3M) is the same as that used in Liao's work.

1.5.2 Rayleigh damping

The GHM method introduced in the previous section only provides us with a approach to model the passive damping due to the viscoelastic materials in the ACL/EACL systems. But in dynamic analysis, the damping comes from structures (inherent energy dissipation in structure other than VEM) also plays an important role. Here, the most convenient approach to model this damping is to use Rayleigh damping that is proportional to the mass and stiffness of the structure.

The major advantage in using Rayleigh damping as a part of the total system damping matrix lies in the fact that, using orthogonal transformation, a structure having n degrees of freedom ($n > 1000$ in the model developed in this research) can be reduced to n uncoupled equations as follows

$$\begin{aligned}
&2\xi_1\omega_1 = \alpha + \beta\omega_1^2 \\
&2\xi_2\omega_2 = \alpha + \beta\omega_2^2 \\
&\cdots \\
&2\xi_r\omega_r = \alpha + \beta\omega_r^2 \\
&\cdots \\
&2\xi_l\omega_l = \alpha + \beta\omega_l^2 \\
&\cdots \\
&2\xi_n\omega_n = \alpha + \beta\omega_n^2
\end{aligned} \tag{1.5.1}$$

where ξ and ω denote the modal damping ratio and frequency.

We can pick $[\omega_r, \omega_l]$ as the frequency range to be studied, or, we can pick up two of the most significant modes of the total structure. The system can be approximately reduced to

$$\begin{aligned}
&2\xi_r\omega_r = \alpha + \beta\omega_r^2 \\
&2\xi_l\omega_l = \alpha + \beta\omega_l^2
\end{aligned} \tag{1.5.2}$$

By solving Eq. (1.5.2), the Rayleigh damping constants can be obtained.

1.6 Thesis Objectives and Outline

The objectives of this research are to develop models for two dimensional plate structures with the EACL/ACL treatments, and implement the EACL treatment on plate structure. This thesis consists of six chapters.

In Chapter 1, background and literature review on related research are introduced.

In Chapter 2, a detailed finite element model of the EACL treated cantilever plate is developed. The seven-DOF, rectangular elements are used to model the ACL patch and edge elements. GHM method and Rayleigh damping are used to model the system damping.

In Chapter 3, the model developed in Chapter 2 is experimentally validated. The simulation results for the ACL treated cantilever beam, clamped-clamped plate with fully covered ACL, cantilever plate with ACL/EACL are compared with the experimental data.

In Chapter 4, numerical examples on parametric study are given. The location of the EACL patch is investigated. Both passive damping ability and active control authority are considered.

In Chapter 5, the EACL treated plate is implemented. The effectiveness of the EACL patch is tested. The PPF controller is introduced to generate the control signal. The vibration performances of the ACL and EACL systems are compared. The simulation result of the closed loop system is also compared with the experimental data at the end of this chapter.

Finally in Chapter 6, conclusion and future work are summarized.

CHAPTER TWO

SYSTEM MODELING

In this chapter, a detailed finite element modeling procedure of a clamp-free (cantilever) plate with partially covered active constrained layer (ACL) and enhanced active constrained layer (EACL) is given. The finite element model of the EACL treated beam was developed by Liao and Wang [1998]. The finite element model for the fully covered ACL plate was developed by Jo and Baz [1999]. The model developed in this thesis is based on their works. The major differences are as follows:

(1) Liao and Wang's one dimensional model is expanded to 2D structure. (beam to plate)

(2) For the plate structure, modeling edge elements is more complicated than that for the beam.

(3) Rayleigh damping and the Golla-Hughes-McTavish (GHM) method are used in this model; in Jo and Baz's model, no structure damping was introduced and complex shear modulus was used for viscoelastic materials.

(4) In Jo and Baz's model, the plate is fully covered with PVDF/VEM layers. In this model, the plate is partially covered with an ACL/EACL patch, thus the location of this patch can be discussed for suppressing different vibration modes.

2.1 Assumptions

The plate elements used here in the ACL/EACL finite element model are 2D rectangular elements based on following assumptions:

(1) The shear strains in the piezoelectric layer and the base plate are negligible.

(2) The transverse displacement w of all points on any cross section of the sandwiched plate is considered to be the same.

(3) The density and thickness are uniform in each layer.

(4) The viscoelastic damping layer is assumed to be linear and is modeled with GHM method.

(5) The top piezoelectric layer (the constraining layer), the viscoelastic layer (the core) and the base plate are perfectly bonded.

(6) Plane section normal to the mid-plane before bending, remains plane after bending in each layer.

2.2 *Elements*

Rectangular elements are used here in the FEM model. Both in-plane stretch and bending effect are considered. As shown in Figure 2.2.1 and 2.2.2, there are four nodes for each rectangular element. Each node has five degrees of freedoms $\{u_3, v_3, w, w_x, w_y\}$ for the pure base plate element and seven DOFs $\{u_1, v_1, u_3, v_3, w, w_x, w_y\}$ for the ACL patch element and the EACL element. The subscripts 1 and 3 refer to the piezoelectric layer and base structure respectively. The notations u_1, v_1, u_3 and v_3 represent the in-plane displacements of the constraining layer and the base structure; w, w_x and w_y represent the transverse displacements of all layers and the slopes of the deflection lines.

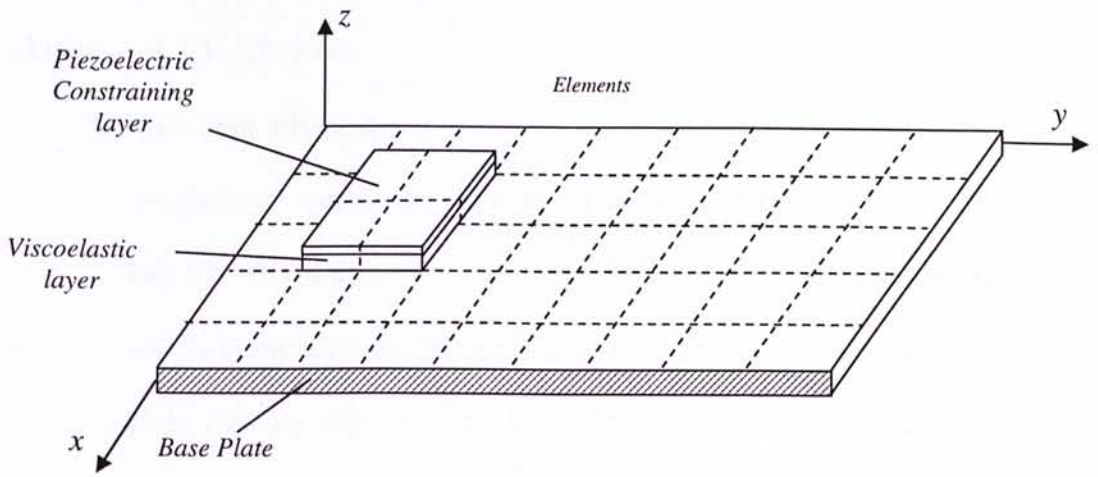

Figure 2.2.1 Coordinate system of the cantilever plate with finite elements

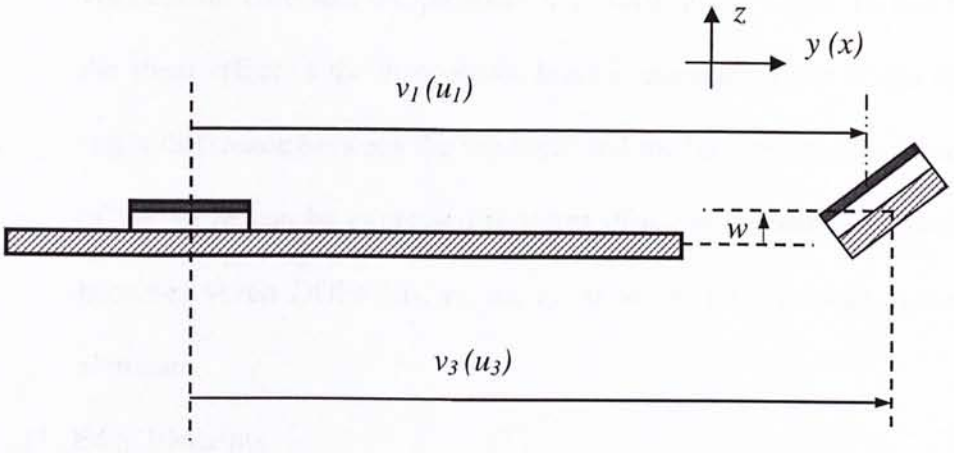

Figure 2.2.2 Undeflected cross section and deflected cross section

More details for choosing finite elements are given as follows.

For the plate partially covered with ACL/EACL, three types of elements are used (Figure 2.2.3). They are

(1) Plain Plate Elements

Single layer rectangular elements. Four nodes per element and each node has five DOFs $\{u_3, v_3, w, w_x, w_y\}$. Although there are in-plane DOFs u_3 and v_3 in the element, in most cases, the bending and torsion effect of the plate (mainly described by three DOFs, w, w_x and w_y) dominates the whole mechanical vibration, which means the in-plane displacement in this region can be ignored.

(2) ACL Elements

Double layer rectangular elements. There are seven DOFs per node. Physically, there're three layers in the ACL patched area: base plate,

viscoelastic core and the piezoelectric constraining layer. In this model, the shear effect of the viscoelastic layer is considered due to the in-plane strain difference between the top layer and the base plate. The shear strain of the VEM can be expressed in terms of u_1, v_1, u_3 and v_3. Therefore, it becomes seven DOFs $\{u_1, v_1, u_3, v_3, w, w_x, w_y\}$ for a node in the ACL elements.

(3) Edge Elements

Double layer rectangular elements. There are seven DOFs, $\{u_1, v_1, u_3, v_3, w, w_x, w_y\}$, per node. The Edge Elements are similar to the ACL elements. The viscoelastic core is replaced by epoxy glue. Different from the VEM, the epoxy glue has much higher shear modulus. It should be noted that the GHM formulation for modeling the VEM will be removed for the epoxy.

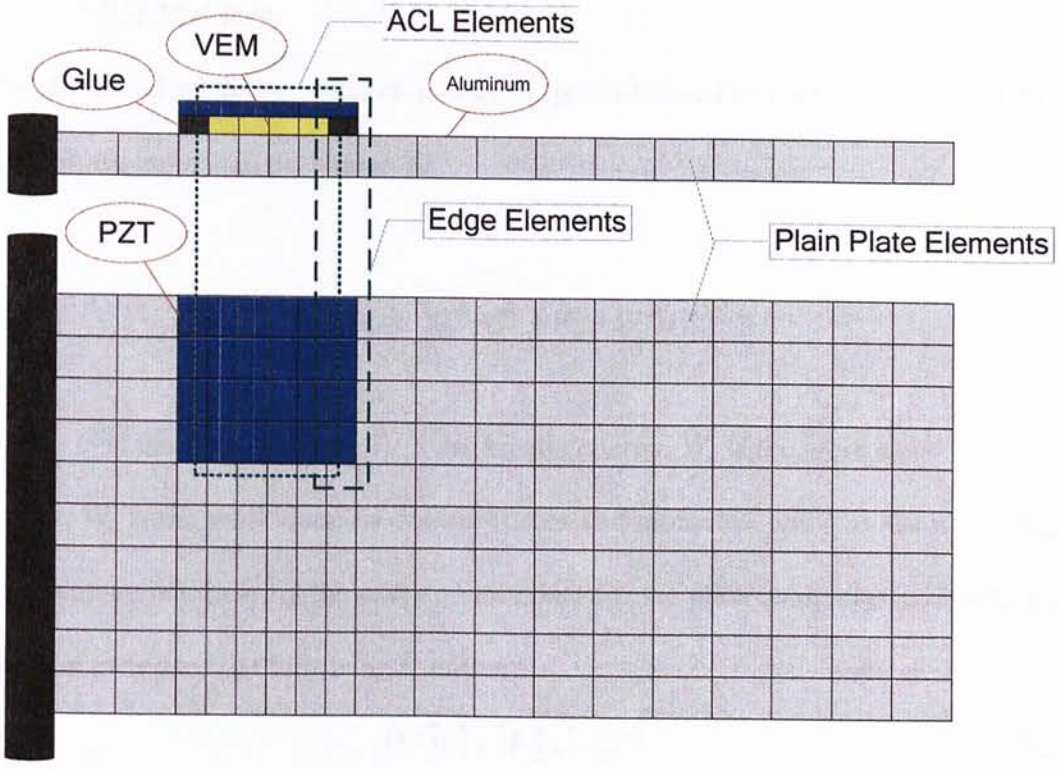

Figure 2.2.3 Finite element mesh and element types

2.3 *FEM Matrices*

By the standard finite element modeling procedures, the energy functional of the structural system can be written as:

$$\pi_p = \int_v (U - T_k + W_e + W_c) dV \tag{2.3.1}$$

where U is the strain energy, T_k is the kinetic energy, W_e is the work done by external forces, W_c is the work done by control forces and moments, and V is the total volume of the plate. Minimizing the energy functional for the plate using classical variational method generates the following equation:

$$[M][\ddot{u}] + [K][u] = [F] \tag{2.3.2}$$

where M, K, and F denote the system mass matrix, stiffness matrix, and excitation/ control forces and moments, respectively.

2.3.1 Element matrices component related to in-plane displacement

For the in-plane deformation, the vibration can be analysed by dividing the plate up into an assemblage of two dimensional elements (thin plate elements) of constant thickness, h, which is subject to distributed boundary loads, called membrane elements. Here a mostly common shape of element, the rectangular element is used (Figure 2.3.1).

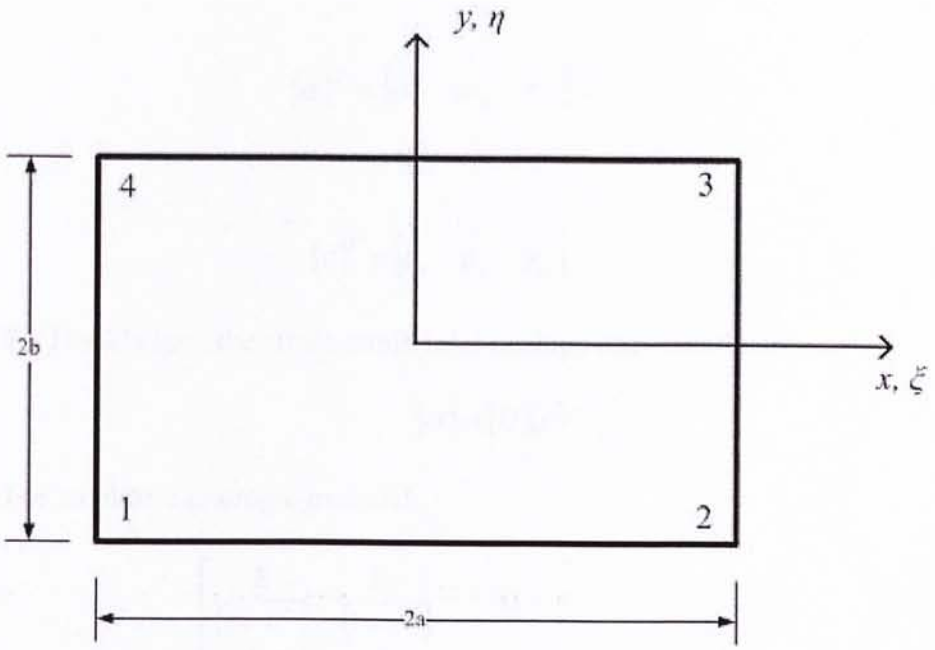

Figure 2.3.1 Geometry of the rectangular element ($\xi=x/a$, $\eta=y/b$)

These loads are applied in directions that are parallel to the middle plane of the plate and uniformly distributed through the thickness. The state stress is defined by the components σ_x, σ_y, $\tau_{xy,}$ which are assumed to be independent of z. Such a state is called 'plane stress' and this 'membrane element' is one of the two types of element components used in the model studied here.

The strain energy (potential energy) stored in the element is given by

$$U = \frac{1}{2}\int_v \left(\sigma_x \varepsilon_x + \sigma_y \varepsilon_y + \tau_{xy}\gamma_{xy}\right) dV \tag{2.3.3}$$

We can rewrite it in compact form

$$U = \frac{1}{2}\int_v \{\sigma\}^T \{\varepsilon\} dV \tag{2.3.4}$$

where

$$\{\sigma\}^T = \begin{bmatrix} \sigma_x & \sigma_y & \tau_{xy} \end{bmatrix} \tag{2.3.5}$$

and

$$\{\varepsilon\}^T = \begin{bmatrix} \varepsilon_x & \varepsilon_y & \gamma_{xy} \end{bmatrix} \tag{2.3.6}$$

By Hook's law, the stress-strain relationships can be expressed as

$$\{\sigma\} = [D]\{\varepsilon\} \tag{2.3.7}$$

For an elastic isotropic material,

$$[D] = \begin{bmatrix} \frac{E}{(1-\nu^2)} & \frac{E\nu}{(1-\nu^2)} & 0 \\ \frac{E\nu}{(1-\nu^2)} & \frac{E}{(1-\nu^2)} & 0 \\ 0 & 0 & G \end{bmatrix} \tag{2.3.8}$$

where

$$G = \frac{E}{2(1+\nu)} \tag{2.3.9}$$

is the shear modulus and E is the material Young's modulus and ν is the Poisson ratio.

Substituting Equation (2.3.7) into the energy function (2.3.4), we obtain

$$U = \frac{1}{2}\int_V \{\varepsilon\}^T [D]\{\varepsilon\} dV \tag{2.3.10}$$

Since the strain and stress are not varying along z. We can change the integration from volume to area

$$U = \frac{1}{2} h \int_A \{\varepsilon\}^T [D]\{\varepsilon\} dA \tag{2.3.11}$$

We can express the strains in Equation (2.3.10) in terms of displacements

$$\{\varepsilon\}=\begin{bmatrix} \partial u/\partial x \\ \partial v/\partial y \\ \partial u/\partial y+\partial v/\partial x \end{bmatrix} \tag{2.3.12}$$

Now, we can write the kinetic energy of the membrane element as

$$T=\frac{1}{2}\int_A \rho h\left(\dot{u}^2+\dot{v}^2\right)dA \tag{2.3.13}$$

Let us go back to the element. By defining shape functions, for each element, displacement can be expressed with nodal displacements

$$u=\sum_{j=1}^{4} N_j u_j \qquad \text{j=1, 2, 3, 4} \tag{2.3.14}$$

$$v=\sum_{j=1}^{4} N_j v_j \qquad \text{j=1, 2, 3, 4} \tag{2.3.15}$$

or

$$\begin{bmatrix} u \\ v \end{bmatrix}=\begin{bmatrix} N_1 & 0 & N_2 & 0 & N_3 & 0 & N_4 & 0 \\ 0 & N_1 & 0 & N_2 & 0 & N_3 & 0 & N_4 \end{bmatrix}\begin{bmatrix} u_1 \\ v_1 \\ u_2 \\ v_2 \\ u_3 \\ v_3 \\ u_4 \\ v_4 \end{bmatrix} \tag{2.3.16}$$

or

$$\begin{bmatrix} u \\ v \end{bmatrix}=[N]\{u\}_e \tag{2.3.17}$$

From the geometry, we can derive the shape functions in above equations as follows:

$$
\begin{aligned}
N_1 &= \frac{1}{4}(1-\xi)(1-\eta) \\
N_2 &= \frac{1}{4}(1+\xi)(1-\eta) \\
N_3 &= \frac{1}{4}(1+\xi)(1+\eta) \\
N_4 &= \frac{1}{4}(1-\xi)(1+\eta)
\end{aligned}
\tag{2.3.18}
$$

If we define two non-dimensional coordinates $\xi = x/a$ and $\eta = y/b$, we can rewrite the above shape functions in the non-dimensional form

$$
N_j = \frac{1}{4}(1-\xi_j\xi)(1+\eta_j\eta) \tag{2.3.19}
$$

where j = 1, 2, 3, 4 and (ξ_j , η_j) is (-1, -1), (1, -1), (1, 1) and (-1, 1) from node 1 to node 4, respectively.

As defined in Section 3.2, for each node

$$
\{u\}^T_{node} = [u_1, v_1, u_3, v_3, w, w_x w_y] \tag{2.3.20}
$$

Here only the in-plane vibration (without bending) is considered, so we can make room for the unused vertical coordinates and write the element shape function as

$$
N = \begin{bmatrix} N^1_u \\ N^1_v \\ N^3_u \\ N^3_v \end{bmatrix} \tag{2.3.21}
$$

with

$$N_u^1 =$$
$$[N_1\ 0\ 0\ 0\ 0\ 0\ 0\ N_2\ 0\ 0\ 0\ 0\ 0\ 0\ N_3\ 0\ 0\ 0\ 0\ 0\ 0\ N_4\ 0\ 0\ 0\ 0\ 0\ 0]$$

$$N_v^1 =$$
$$[0\ N_1\ 0\ 0\ 0\ 0\ 0\ 0\ N_2\ 0\ 0\ 0\ 0\ 0\ 0\ N_3\ 0\ 0\ 0\ 0\ 0\ 0\ N_4\ 0\ 0\ 0\ 0\ 0]$$

$$N_u^3 =$$
$$[0\ 0\ N_1\ 0\ 0\ 0\ 0\ 0\ 0\ N_2\ 0\ 0\ 0\ 0\ 0\ 0\ N_3\ 0\ 0\ 0\ 0\ 0\ 0\ N_4\ 0\ 0\ 0\ 0]$$

$$N_v^3 =$$
$$[0\ 0\ 0\ N_1\ 0\ 0\ 0\ 0\ 0\ 0\ N_2\ 0\ 0\ 0\ 0\ 0\ 0\ N_3\ 0\ 0\ 0\ 0\ 0\ 0\ N_4\ 0\ 0\ 0]$$

(2.3.22)

where superscript *1* denotes the constraining layer while *3* denotes the base plate. The subscripts *1-4* denote the node number of the element.

If we substitute Equation (2.3.21) into Equation (2.3.13), it turns out

$$T_e = \frac{1}{2}\{\dot{u}\}_e^T [M]_e \{\dot{u}\}_e \tag{2.3.23}$$

where

$$[M]_e = \int_{A_e} \rho h [N]^T [N] dA \tag{2.3.24}$$

We can obtain the final mass matrix containing all three layers from Equations (2.3.21) and (2.3.24) as follows

$$[M_{in-plane}] = \rho_1 h_1 \int_{-1}^{+1}\int_{-1}^{+1}\left(\{N_u^1\}^T\{N_u^1\} + \{N_v^1\}^T\{N_v^1\}\right)d\xi d\eta$$

$$+ \rho_3 h_3 \int_{-1}^{+1}\int_{-1}^{+1}\left(\{N_u^3\}^T\{N_u^3\} + \{N_v^3\}^T\{N_v^3\}\right)d\xi d\eta \qquad (2.3.25)$$

$$+\frac{1}{4}\rho_2 h_2 \int_{-1}^{+1}\int_{-1}^{+1}\left(\begin{array}{l}\left\{\begin{array}{l}\int\left(\{N_u^1\}+\{N_u^3\}\right)\\ \left|+h\{N_w\}_{,x}\right|\end{array}\right\}^T\left\{\begin{array}{l}\int\left(\{N_u^1\}+\{N_u^3\}\right)\\ \left|+h\{N_w\}_{,x}\right|\end{array}\right\}\\ +\left\{\begin{array}{l}\int\left(\{N_v^1\}+\{N_v^3\}\right)\\ \left|+h\{N_w\}_{,y}\right|\end{array}\right\}^T\left\{\begin{array}{l}\int\left(\{N_v^1\}+\{N_v^3\}\right)\\ \left|+h\{N_w\}_{,y}\right|\end{array}\right\}\end{array}\right)d\xi d\eta$$

where the first part relates to constraining layer, the second part relates to the base plate while the last part is associated with the viscoelastic layer. ρ_j in the above equation represent the material density of the j^{th} layer.

It should be noted that all nodal displacements related to the viscoelastic layer (the third part) are derived from the nodal displacement relationship between the constraining layer and the base structure. The relationship and description of N_w (the bending shape function) are given in detail in following sections.

Thus Equation (2.3.25) is the first component of the element mass matrix.

Similarly, if we substitute Equation (2.3.21) into Equation (2.3.11), it turns out

$$U_e = \frac{1}{2}\{u\}_e^T[K]_e\{u\}_e \qquad (2.3.26)$$

where the desired element stiffness matrix is obtained as

$$[K]_e = \int_{A_e} h[B]^T[D][B]dA \qquad (2.3.27)$$

where

$$[B]=\begin{bmatrix} \partial/x & 0 \\ 0 & \partial/y \\ \partial/y & \partial/x \end{bmatrix}[N] \tag{2.3.28}$$

From Equation (2.3.21), the in-plane stiffness matrix of each layer is given by

$$\left[K_{in-plane}\right]=h_j\int_{-1}^{+1}\int_{-1}^{+1}\left[B_p^j\right]^T\left[D_p^j\right]\left[B_p^j\right]d\xi d\eta, \qquad j=layer\ \ 1,\ \ 2\ \ and\ \ 3 \tag{2.3.29}$$

where $\left[B_p^j\right]$ and $\left[D_p^j\right]$ are derived from Equations (2.3.22) and (2.3.9)

$$\left[B_p^j\right]=\begin{bmatrix} \left\{N_u^j\right\}_{,x} \\ \left\{N_v^j\right\}_{,y} \\ \left\{N_u^j\right\}_{,y}+\left\{N_v^j\right\}_{,x} \end{bmatrix} \tag{2.3.30}$$

$$\left[B_p^2\right]=\begin{bmatrix} \left\{N_u^1\right\}_{,x}+\left\{N_u^3\right\}_{,x}+h\left\{N_w\right\}_{,xx} \\ \left\{N_v^1\right\}_{,y}+\left\{N_v^3\right\}_{,y}+h\left\{N_w\right\}_{,yy} \\ \left\{N_u^1\right\}_{,y}+\left\{N_u^3\right\}_{,y}+h\left\{N_w\right\}_{,yx}+\left\{N_v^1\right\}_{,x}+\left\{N_v^3\right\}_{,x}+h\left\{N_w\right\}_{,xy} \end{bmatrix} \tag{2.3.31}$$

$$\left[D_p^j\right]=\frac{E_j}{1-\upsilon_j^2}\begin{bmatrix} 1 & \nu_j & 0 \\ \nu_j & 1 & 0 \\ 0 & 0 & \dfrac{1-\nu_j}{2} \end{bmatrix} \tag{2.3.32}$$

where h = $(h_1-h_3)/2$; $j=layer$ 1 *and* 3 ; E_j , ν_j and h_j denote the Young's Modulus, Poisson ratio and thickness of the j[th] layer.

2.3.2 *Element matrices component related to bending displacement*

As shown in Figure 2.3.2, a non-conforming rectangular bending element is used here as another component of the total element.

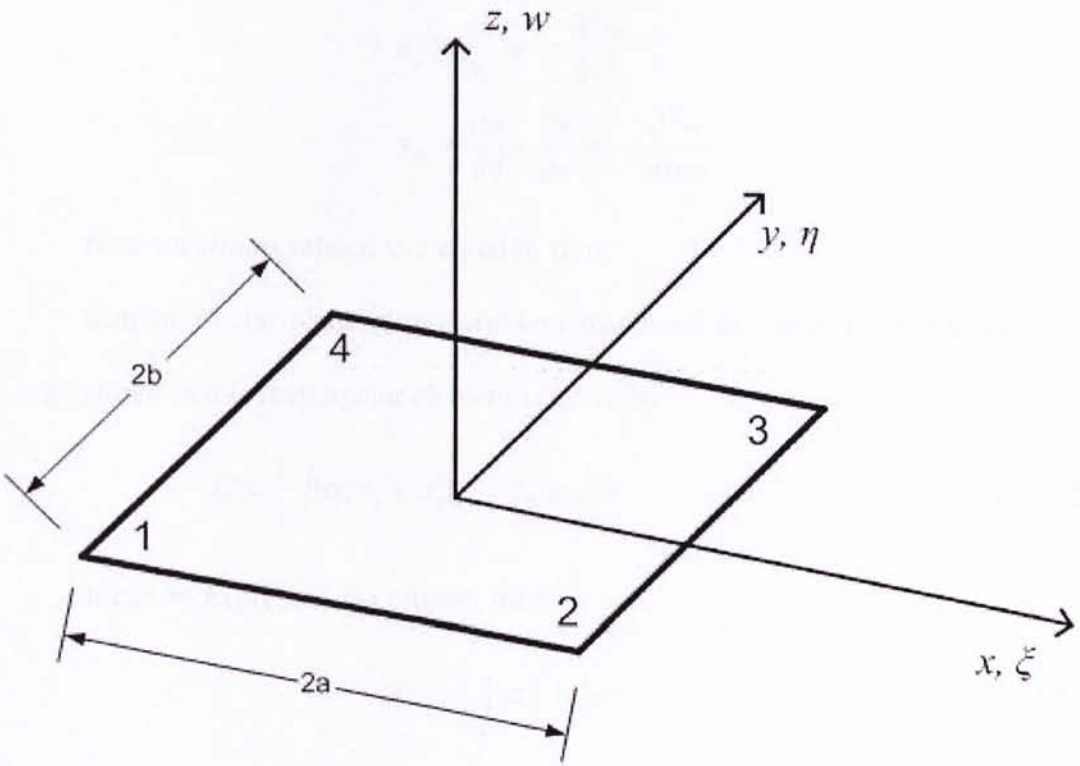

Figure 2.3.2 Geometry of a rectangular bending element ($\xi=x/a$, $\eta=y/b$)

The first step is to derive the energy functions. In this thin plate bending element, it is assumed that the direct stress in the transverse direction, σ_z, is zero. Thus, the displacements parallel to the middle surface of the plate are given by

$$\begin{aligned} u(x,\ y,\ z) &= -z\frac{\partial w}{\partial x} \\ v(x,\ y,\ z) &= -z\frac{\partial w}{\partial y} \end{aligned} \tag{2.3.33}$$

where $w(x, y)$ is the vertical displacement of all layers.

Following the definition of strain and Equation (2.3.32), we have

$$\begin{aligned}\varepsilon_x &= \frac{\partial u}{\partial x} = -z\frac{\partial^2 w}{\partial x^2} \\ \varepsilon_y &= \frac{\partial v}{\partial y} = -z\frac{\partial^2 w}{\partial y^2} \\ \gamma_{xy} &= \frac{\partial u}{\partial y} + \frac{\partial v}{\partial x} = -z\frac{\partial^2 w}{\partial x \partial y}\end{aligned} \tag{2.3.34}$$

Note all strains related to z equal to zero.

Similar to the plane stress problem discussed in Section 3.3, the potential energy stored in this rectangular element is given by

$$U = \frac{1}{2}\int_v \left(\sigma_x \varepsilon_x + \sigma_y \varepsilon_y + \tau_{xy}\gamma_{xy}\right) dV \tag{2.3.35}$$

It can be expressed in compact form

$$U = \frac{1}{2}\int_v \{\sigma\}^T \{\varepsilon\} dV \tag{2.3.36}$$

where

$$\{\sigma\}^T = \begin{bmatrix}\sigma_x & \sigma_y & \tau_{xy}\end{bmatrix} \tag{2.3.37}$$

Since the z-related stress is zero, by Hook's law, the stress-strain relationship can be expressed as

$$\{\sigma\} = [D]\{\varepsilon\} \tag{2.3.38}$$

where $[D]$ is given by Equation (2.3.9).

Substituting Equation (2.3.38) into the energy function (2.3.35), we can obtain

$$U = \frac{1}{2}\int_v \{\varepsilon\}^T [D]\{\varepsilon\} dV \tag{2.3.39}$$

Using Equation (2.3.33), Equation (2.3.39) can be expressed in terms of displacements

$$U = \frac{1}{2}\int_V z^2 \begin{bmatrix} \partial^2 w/\partial x^2 \\ \partial^2 w/\partial y^2 \\ \partial^2 w/\partial x \partial y \end{bmatrix}^T [D] \begin{bmatrix} \partial^2 w/\partial x^2 \\ \partial^2 w/\partial y^2 \\ \partial^2 w/\partial x \partial y \end{bmatrix} dV \tag{2.3.40}$$

Integrating the above equation with respect to z along the thickness h turns out

$$U = \frac{1}{2}\int_A \frac{h^3}{12} \begin{bmatrix} \partial^2 w/\partial x^2 \\ \partial^2 w/\partial y^2 \\ \partial^2 w/\partial x \partial y \end{bmatrix}^T [D] \begin{bmatrix} \partial^2 w/\partial x^2 \\ \partial^2 w/\partial y^2 \\ \partial^2 w/\partial x \partial y \end{bmatrix} dA \tag{2.3.41}$$

Also, in terms of displacements, we can write the kinetic energy of the bending element as

$$T = \frac{1}{2}\int_A \rho h \dot{w}^2 dA \tag{2.3.42}$$

Now we go back to the element again. There are three degrees of freedom at each node, which are the displacement w, and two rotations

$$\begin{aligned} \theta_x &= \partial w/\partial y \\ \theta_y &= -\partial w/\partial x \end{aligned} \tag{2.3.43}$$

If we rewrite it in terms of the non-dimensional coordinates, we obtain

$$\begin{aligned} \theta_x &= \frac{1}{b}\frac{\partial w}{\partial \eta} \\ \theta_y &= -\frac{1}{a}\frac{\partial w}{\partial \xi} \end{aligned} \tag{2.3.44}$$

We define

$$w = \begin{bmatrix} N_{w1} & N_{w2} & N_{w3} & N_{w4} \end{bmatrix} \begin{bmatrix} w_1 \\ \theta_{x1} \\ \theta_{y1} \\ \vdots \\ w_4 \\ \theta_{x4} \\ \theta_{y4} \end{bmatrix} = [N_w]\{w\}_e \tag{2.3.45}$$

where the shape functions are given by

$$N_{wj}{}^T = \begin{bmatrix} \frac{1}{8}(1+\xi_j\xi)(1+\eta_j\eta)(2+\xi_j\xi+\eta_j\eta-\xi^2-\eta^2) \\ \frac{b}{8}(1+\xi_j\xi)(\eta_j+\eta)(\eta^2-1) \\ \frac{a}{8}(1+\eta_j\eta)(\xi_j+\xi)(\xi^2-1) \end{bmatrix} \tag{2.3.46}$$

$$j = 1,2,3,4$$

Hence, if we make room for four in-plane coordinates (u_1, v_1, u_3 and v_3) in the shape function matrix, we can rewrite N_w as

$$[N_w] = [0 \quad 0 \quad 0 \quad 0 \quad N_{w1} \quad 0 \quad 0 \quad 0 \quad 0 \quad N_{w2} \quad 0 \quad 0 \quad 0 \quad 0 \quad N_{w3} \quad 0 \quad 0 \quad 0 \quad N_{w4}] \tag{2.3.47}$$

If we substitute Equation (2.3.47) into Equation (2.3.42), we get

$$T_e = \frac{1}{2}\{\dot{w}\}_e^T [M]_e \{\dot{w}\}_e \tag{2.3.48}$$

where

$$[M]_e = \int_{A_e} \rho h [N_w]^T [N_w] dA \tag{2.3.49}$$

Considering the whole three layers with the use of non-dimensional coordinates, the bending mass matrix is

$$[M_{bending}]=(\rho_1 h_1+\rho_2 h_2+\rho_3 h_3)\int_{-1}^{+1}\int_{-1}^{+1}[N_w]^T[N_w]d\xi d\eta \tag{2.3.50}$$

where ρ_j is the density of the jth layer.

Similarly, by substituting Equation (2.3.47) into Equation (2.3.41), we obtain

$$U_e=\frac{1}{2}\{w\}_e^T[K]_e\{w\}_e \tag{2.3.51}$$

where

$$[K]_e=\int_{A_e}\frac{h^3}{12}[B]^T[D][B]dA \tag{2.3.52}$$

Again, considering the whole three layers with ξ and η, the bending stiffness matrix is obtained as

$$[K_{bending}]=\int_{-1}^{+1}\int_{-1}^{+1}[B_b]^T[D_b^j][B_b]d\xi d\eta$$
$$j=\ 1,\ \ 2\ \ and\ \ 3 \tag{2.3.53}$$

with

$$[B_b]=\begin{bmatrix}\{N_w\}_{,xx}\\ \{N_w\}_{,yy}\\ 2\{N_w\}_{,xy}\end{bmatrix} \tag{2.3.54}$$

$$\left[D_b^j\right]=\frac{E_j I_j}{1-\upsilon_j^2}\begin{bmatrix} 1 & \upsilon_j & 0 \\ \upsilon_j & 1 & 0 \\ 0 & 0 & \dfrac{1-\upsilon_j}{2} \end{bmatrix} \qquad (2.3.55)$$

$$j = 1,\ 2 \ \textit{and}\ \ 3$$

where I_j , E_j , υ_j and h_j in the above equations denote the area moment of inertia, Young's Modulus, Poisson ratio and thickness of the j^{th} layer.

2.3.3 Element matrices component related to shear strain

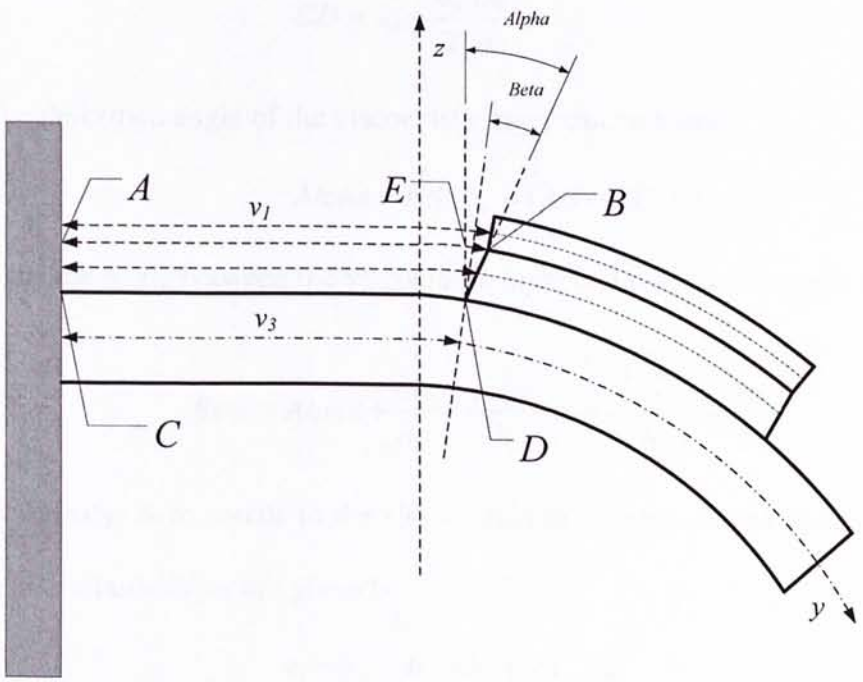

Figure 2.3.3 Geometry of displacements and VEM shear strains

From the classical plate theory together with assumptions (a)-(g), the cantilever plate follows

$$\theta_x = \partial w/\partial y$$
$$\theta_y = -\partial w/\partial x \tag{2.3.56}$$

The relationship between nodal displacements and VEM shear strains γ_{xz} and γ_{yz} can be found from Figure 2.3.3

The mid-plane nodal position of the constraining layer is

$$AB = v_1 + \frac{h_c}{2}\frac{\partial w}{\partial y} \tag{2.3.57}$$

The mid-plane nodal position of the base plate is

$$CD = v_3 - \frac{h_b}{2}\frac{\partial w}{\partial y} \tag{2.3.58}$$

The deformed angle of the viscoelastic layer can be found

$$Alpha = EB / h_v = (AB - CD) / h_v \tag{2.3.59}$$

Thus the angle between the viscoelastic layer and the base structure is

$$Beta = Alpha + \frac{\partial w}{\partial y} = \frac{v_1 - v_3}{h_v} + \frac{\frac{h_c}{2} + \frac{h_b}{2} + h_v}{h_v}\frac{\partial w}{\partial y} \tag{2.3.60}$$

Obviously, *Beta* equals to the shear strain in y direction and finally the shear strains in viscoelastic layer are given by

$$\gamma_{xz} = \frac{u_1 - u_3}{h_2} + \frac{h_c + h_b + 2h_v}{2h_2}\frac{\partial w}{\partial x} \tag{2.3.61}$$

$$\gamma_{yz} = \frac{v_1 - v_3}{h_v} + \frac{h_c + h_b + 2h_v}{2h_v}\frac{\partial w}{\partial y} \tag{2.3.62}$$

where h_c, h_b and h_v denote the thickness of constraining layer, base plate and viscoelastic layer, respectively.

The strain energy due to the shear deformation stored in the element is given by

$$U = \frac{1}{2}\int_v \{\tau\}^T \{\gamma\} dV \tag{2.3.63}$$

where

$$\{\tau\} = \begin{bmatrix} \tau_{xz} \\ \tau_{yz} \end{bmatrix} \tag{2.3.64}$$

$$\{\gamma\} = \begin{bmatrix} \gamma_{xz} \\ \gamma_{yz} \end{bmatrix} \tag{2.3.65}$$

Substitute Equation (2.3.62) into Equation (2.3.64) with the Hook's law, it results in

$$\{\tau\} = G\{\gamma\} = \frac{E}{2(1+\nu)} \begin{Bmatrix} \dfrac{u_1 - u_3}{h_2} + \dfrac{h_c + h_b + 2h_v}{2h_2}\dfrac{\partial w}{\partial x} \\ \dfrac{v_1 - v_3}{h_v} + \dfrac{h_c + h_b + 2h_v}{2h_v}\dfrac{\partial w}{\partial y} \end{Bmatrix} \tag{2.3.66}$$

Equation (2.3.63) can be rewritten as

$$U = \frac{1}{2} G \int_v \{\gamma\}^T \{\gamma\} dV \tag{2.3.67}$$

Thus, by substituting Equations (2.3.21) and (2.3.47) into Equation (2.3.67), we can derive the shear stiffness matrix as

$$[K_{shear}] = G_2 h_2 \int_{-1}^{+1}\int_{-1}^{+1} [B_2]^T [B_2] d\xi d\eta \tag{2.3.68}$$

with

$$[B_2]=\frac{d}{h_2}\begin{bmatrix}(\{N_u^1\}-\{N_u^3\})/d+\{N_w\}_{,x}\\(\{N_v^1\}-\{N_v^3\})/d+\{N_w\}_{,y}\end{bmatrix} \tag{2.3.69}$$

where the shape functions are given in previous sections and

$$d=(h_2+h_1/2+h_3/2) \tag{2.3.70}$$

2.3.4 Overall element matrices

The element stiffness matrix consists of the three parts discussed in previous sections

$$[K_e]=\lfloor K_{in-plane}\rfloor+[K_{shear}]+\lfloor K_{bending}\rfloor \tag{2.3.71}$$

where $\lfloor K_{in-plane}\rfloor,[K_{shear}]$ and $\lfloor K_{bending}\rfloor$ represent the in-plane stiffness matrix, shear stiffness matrix and the bending stiffness matrix, respectively.

The element mass matrix consists of two parts

$$[M_e]=\lfloor M_{in-plane}\rfloor+\lfloor M_{bending}\rfloor \tag{2.3.72}$$

where $\lfloor M_{in-plane}\rfloor$ and $\lfloor M_{bending}\rfloor$ represent the mass matrix due to in-plane extension, and bending effect, respectively.

2.3.5 *Piezoelectric control forces*

When voltage is applied to the PZT patch, the in-plane stresses and strains will be induced in the piezoelectric layers. As we have

$$T_1 = E_1 \frac{V_a}{h_1} d_{31} \tag{1.1.7}$$

$$T_2 = E_1 \frac{V_a}{h_1} d_{32} \tag{1.1.8}$$

where T_1 and T_2 is the voltage induced stress in x and y direction, E_1 is the Young's modulus of the piezoelectric material, V_a is the applied voltage, h_1 is the thickness of the piezoelectric layer , d_{31} and d_{32} is the piezoelectric constants as discussed in Section 1.1.

Hence, together with element shape functions given before, we can get

$$[F_{PZT}] = V_a \int_{-1}^{+1}\int_{-1}^{+1} [B_p^1]^T [D_p^1] \begin{bmatrix} d_{31} \\ d_{32} \\ 0 \end{bmatrix} d\xi d\eta + V_a \int_{-1}^{+1}\int_{-1}^{+1} [B_b]^T [D_b] \begin{bmatrix} d_{31} \\ d_{32} \\ 0 \end{bmatrix} d\xi d\eta \tag{2.3.73}$$

where the first part is related to the in plane force and the second part is related to the bending stress (moments).

2.4 Damping

2.4.1 Damping due to the viscoelastic materials

Conventionally, the constitutive equation for viscoelastic materials is described by the complex shear modulus such that

$$G^* = G_2 + j\eta G_2 \tag{2.4.1}$$

Generally, the structural dynamics equation can be expressed in the Laplace domain as

$$M_e s^2 q(s) + K_e q(s) + G^* \overline{K} q(s) = f(s) \tag{2.4.2}$$

where M_e and K_e is mass and stiffness matrices contributed from elastic components in the structure, and G^* is given in Equation (2.4.1) as the complex shear modulus of the viscoelastic material.

Modeling the VEM with the complex modulus approach has a shortcoming that can not work directly in time domain but only in frequency domain. However, sometimes it is desired to evaluate the damping effect in time domain as it is more convenient to observe transient phenomena. To overcome this problem, the Golla-Hughes-McTavish (GHM) method is used here [Golla and Hughes, 1985; McTavish and Hughes 1993]. Some background about this method has already introduced in Section 1.5.1.

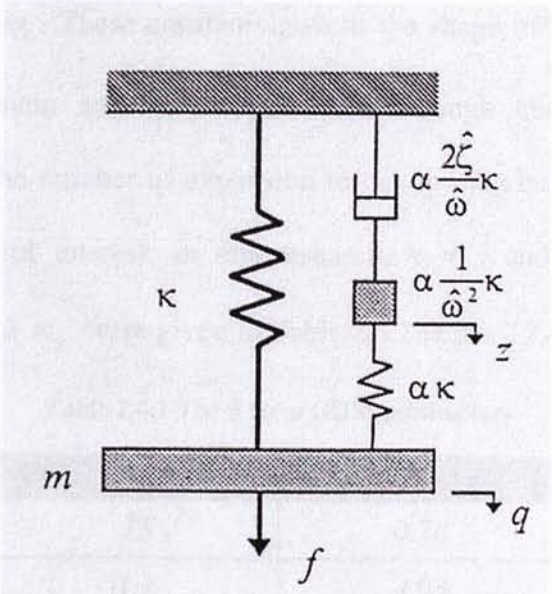

Figure 2.4.1 The mini-oscillator mechanical analogy used in the GHM method (McTavish and Hughes, 1993)

GHM method starts with the Laplace *(s)* domain representation of the material complex modulus as a series of mini-oscillator terms

$$s\tilde{G}(s) = G^{\infty}\left[1+\sum_{k=1}^{n}\alpha_k \frac{s^2+2\xi_k\,\omega_k s}{s^2+2\xi_k\,\omega_k s+\omega_k{}^2}\right] \tag{2.4.3}$$

where G^{∞} is the final value of the relaxation function *G(t)*. The mini-oscillator mechanical analogy used in the GHM method is shown in Figure 2.3.1. This multi-stage damping mechanism can simulate the viscoelastic damping effect over certain frequency range.

Each mini-oscillator term is a second-order rational function with three

constants, α_k ξ_k and ω_k. These constants govern the shape of the modulus function over complex *s*-domain and can be obtained through curve-fitting the VEM experimental data. The number of expansion terms, *n*, may be determined based on the frequency range of interest. In this research, $n = 3$ and those 3 term GHM parameters α_k , ξ_k and ω_k were given in Table 2.4.1 [Liao, 1997].

Table 2.4.1 The 3 term GHM parameters

k	α_k	ξ_k	ω_k
1	*15*	*0.78*	*27967 rad/sec*
2	*1.7*	*4.93*	*22597 rad/sec*
3	*0.52*	*19.45*	*12422 rad/sec*

After some manipulation, the finite element model for the ACL system with the GHM formulation in time domain (n > 1) can be obtained

$$M_v\begin{bmatrix}\ddot{u}(t)\\ \ddot{z}(t)\end{bmatrix}+C_v\begin{bmatrix}\dot{u}(t)\\ \dot{z}(t)\end{bmatrix}+K_v\begin{bmatrix}u(t)\\ z(t)\end{bmatrix}=\begin{bmatrix}F(t)\\ 0\end{bmatrix} \tag{2.4.4}$$

with the GHM viscoelastic matrices given by

$$M_v=\begin{bmatrix} M_e+M_{ev} & 0 & \cdots & 0 \\ 0 & \alpha_1\dfrac{1}{\omega_1^2}G^{\infty}\overline{\Lambda} & 0 & \vdots \\ \vdots & 0 & \ddots & 0 \\ 0 & \cdots & 0 & \alpha_n\dfrac{1}{\omega_n^2}G^{\infty}\overline{\Lambda} \end{bmatrix} \tag{2.4.5}$$

$$C_v=\begin{bmatrix} 0 & 0 & \cdots & 0 \\ 0 & \alpha_1\dfrac{2\xi_1}{\omega_1}G^{\infty}\overline{\Lambda} & 0 & \vdots \\ \vdots & 0 & \ddots & 0 \\ 0 & \cdots & 0 & \alpha_n\dfrac{2\xi_n}{\omega_n}G^{\infty}\overline{\Lambda} \end{bmatrix} \tag{2.4.6}$$

$$K_v = \begin{bmatrix} K_e + K_{ev}\left(1+\sum_{i=1}^{n}\alpha_i\right) & -\alpha_1 \overline{R} G^{\infty} \overline{\Lambda} & \cdots & -\alpha_n \overline{R} G^{\infty} \overline{\Lambda} \\ -\alpha_1 \left(\overline{R} G^{\infty} \overline{\Lambda}\right)^T & \alpha_1 G^{\infty} \overline{\Lambda} & 0 & \vdots \\ \vdots & 0 & \ddots & 0 \\ -\alpha_n \left(\overline{R} G^{\infty} \overline{\Lambda}\right)^T & \cdots & 0 & \alpha_n G^{\infty} \overline{\Lambda} \end{bmatrix} \tag{2.4.7}$$

where M_e and K_e are elastic mass and stiffness matrices; M_{ev} and K_{ev} are mass and stiffness matrices due to the viscoelastic layer in the structure; $\overline{\Lambda}$ is a diagonal matrix of the nonzero eigenvalues of $\overline{K}$, with corresponding eigenvectors forming the columns of $\overline{R}$ so that $\overline{R}^T \overline{R} = I$, $\overline{K} = \overline{R}\overline{\Lambda}\overline{R}^T$. Here, zero eigenvalues that indicate the rigid-body motion modes (there're 6 rigid-body motion modes in the model studied in this thesis) are eliminated to ensure that the viscoelastic mass matrix will be positive definite in the finite element formulation.

2.4.2 *Inherent structural damping*

In the plate partially covered with ACL, besides the viscoelastic damping, the structural damping associated with internal energy dissipation should not be ignored. We can estimate the internal structural damping using the Rayleigh damping as discussed in Section 1.5

$$C_e = \alpha M_e + \beta K_e \tag{2.4.8}$$

where the constants α and β can be determined from experiments. M_e and K_e is the element mass and stiffness matrix, respectively. We can add this damping after the assemblage of system matrices.

Finally, the global GHM-Rayeigh damping matrix can be obtained:

$$C_v = \begin{bmatrix} C_e & 0 & \cdots & 0 \\ 0 & \alpha_1 \frac{2\xi_1}{\omega_1} G^{\infty} \overline{\Lambda} & 0 & \vdots \\ \vdots & 0 & \ddots & 0 \\ 0 & \cdots & 0 & \alpha_n \frac{2\xi_n}{\omega_n} G^{\infty} \overline{\Lambda} \end{bmatrix} \tag{2.4.9}$$

To obtain the values for constants α and β, the frequency domain impulse response of a cantilever plate without ACL/EACL patch is recorded. The damping ratio is estimated from the frequency domain data and the Rayleigh constants are obtained with the natural frequencies and damping ratios of the structure by solving

$$\begin{aligned} 2\xi_L \omega_L &= \alpha + \beta \omega_L^2 \\ 2\xi_H \omega_H &= \alpha + \beta \omega_H^2 \end{aligned} \tag{2.4.10}$$

where ξ_L and ω_L are damping ratio and natural frequency of the lowest structure vibration mode in the frequency range of interest while ξ_H and ω_H are damping ratio and natural frequency of the highest structure vibration mode in the observed frequency range.

2.5 Edge Elements

The edge elements in the EACL treatment are added to improve the actuating ability of the ACL patch. The edge elements were modeled as equivalent springs with stiffness k_{eq} in Liao and Wang's one-dimensional model. In this two-dimensional model, the edge element is modeled as equivalent shear modulus G_{eq}, which is related to the in-plane displacements of the constraining layer and the base plate $\{u_1, v_1, u_3, v_3\}$. Thus, the edge element has 7 DOFs per node, just like the ACL element.

The bending stiffness matrix, in-plane stiffness matrix and mass matrix are the

same as the ACL element. The only difference between the edge element and ACL element exists in the stiffness matrix related to shear

$$[K_{shear}] = G_{eq} h_2 \int_{-1}^{+1} \int_{-1}^{+1} [B_2]^T [B_2] d\xi d\eta \qquad (2.5.1)$$

where G_{eq} can be obtained through experiment.

It should be noted that, as there is no VEM in edge elements, the GHM formulation should not be applied to edge elements; otherwise, it will cause a significant error in damping.

2.6 Model Reduction

The equations discussed in this paper are formulated and solved in MATLAB platform. Comparing with the beam case, the FEM plate model has much more elements, nodes and DOFs. For example, a simple ACL treated plate without edge elements has 150 elements and 176 nodes while each node has 5 or 7 DOFs. Moreover, the GHM method will add hundreds of DOFs more to the global FEM model. Thefore, the finite element model needs to be simplified.

It is understood that the damping effect of the PCL/ACL treatment is effective on higher frequency modes. In one simulation case, it was observed that the modes higher than 400 *Hz* vanished in no more than 0.5 seconds while the amplitudes of these modes are smaller than 1/200 of that of the first mode. Therefore, in this research, only the first 5 or 6 modes are considered by neglecting other higher modes because the first few modes dominate the whole vibration. It should be noted that the DOFs associated with GHM dissipation are kept to ensure the damping is appropriately modeled.

CHAPTER THREE

MODEL VALIDATION

In this chapter, the models developed in Chapter Three will be experimentally validated. In order to validate the models, simulation for the open loop and closed loop responses of different systems will be carried out and compared with experimental results.

Several structural systems will be considered here. One is a beam (one dimensional structure) with passive ACL damping case. The aim of this validation is to test the damping part of the model. Another structure is a clamped-clamped plate with passive ACL damping. The model accuracy is tested under this boundary condition. In this case, the natural frequencies are relatively higher than those of the cantilever plate case performed in our laboratory as the following case. Finally, the cantilever plates with ACL/EACL treatments are analyzed and tested, for both open loop and closed loop.

3.1 Beam with Passive ACL Damping Treatment

Although the model developed in this thesis is for two dimensional structures (plates), it can also be used to describe the behaviours of one dimensional structures (beams).

The experimental setup for testing the ACL/EACL treated beam is shown in Figure 3.1.1. A hammer is used to hit the cantilever beam to perform an impulse test. Both the force input from the hammer and the tip displacement of the beam from the laser vibrometer are input to the FFT analyser to process the data. Figure 3.1.2 and Figure 3.1.3 show the time and frequency responses of the ACL beam system. We can see that both experimental and simulation results match quite well in general.

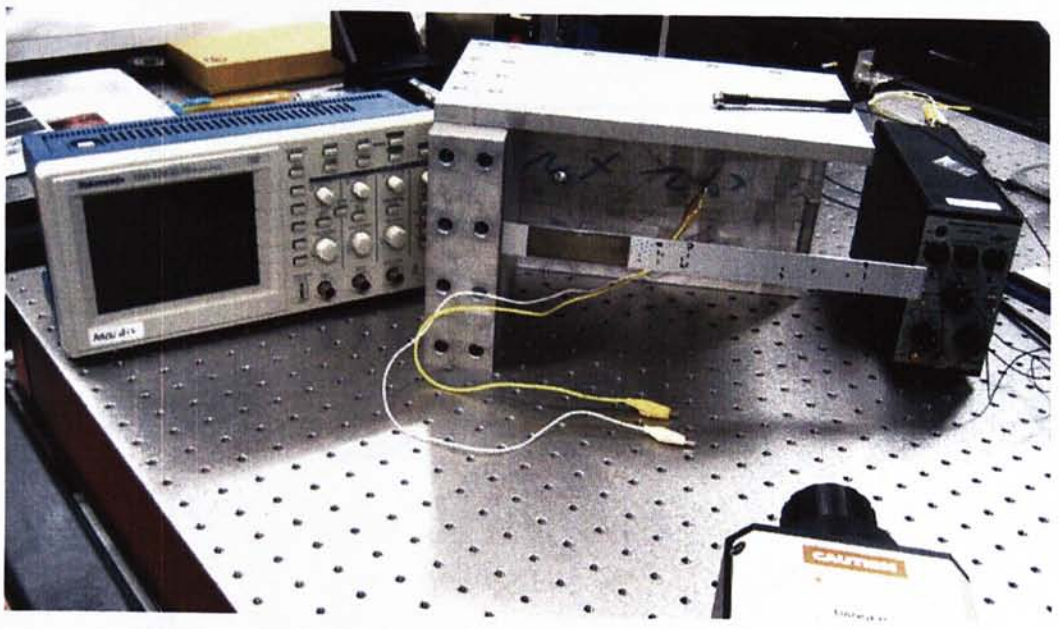

Figure 3.1.1 Experimental setup for testing the passive damping of the beam with ACL

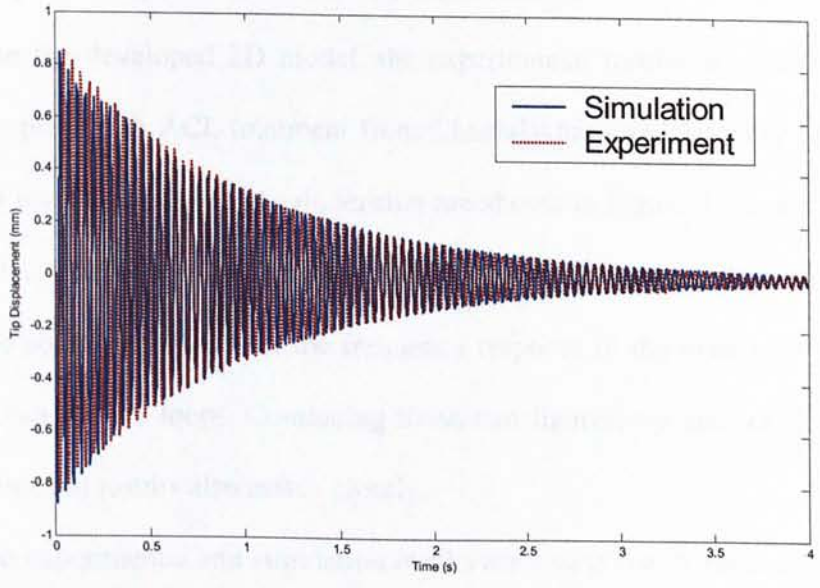

Figure 3.1.2 Time response of tip displacement of the beam

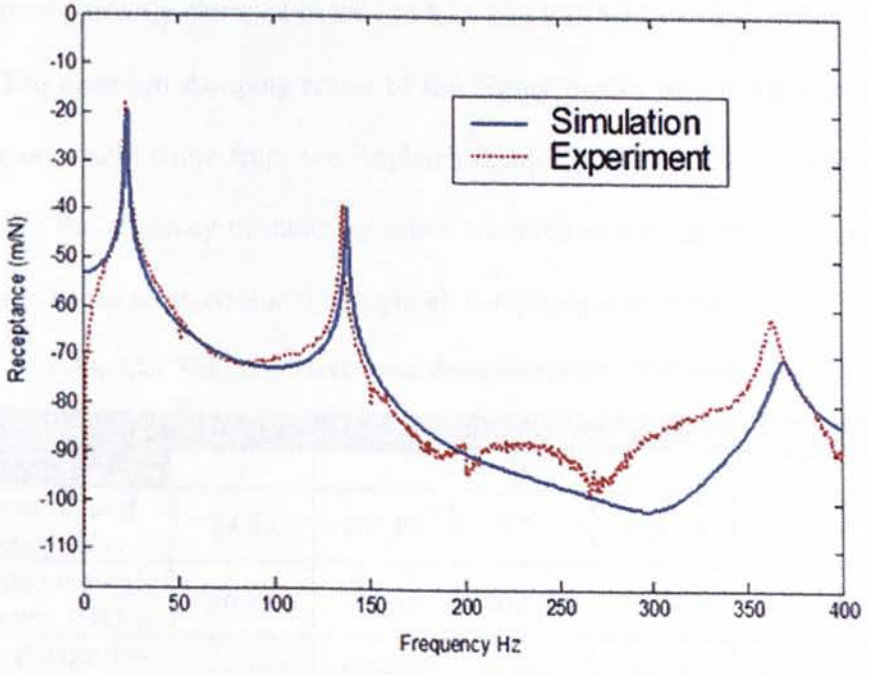

Figure 3.1.3 Frequency response of tip displacement receptance of the beam

3.2 Clamped-Clamped Plate with Fully Covered ACL

To validate the developed 2D model, the experimental results of a clamped-clamped aluminium plate with ACL treatment from Chantalakhana and Stanway (2000) and the simulation results with the same dimension are shown in Figure 3.2.1 and Figure 3.2.2, respectively. The dotted lines in those figures are the frequency response of the plain plate while solid lines represent the frequency response of the plate with fully covered ACL treatment (open loop). Comparing those two figures, we can see both simulation and experimental results also match closely.

The experimental and simulation results are also given in Table 3.2.1 (with ACL damping), from which we can see the errors are acceptable. The measured natural frequencies are lower than the calculated ones probably because the boundary conditions are assumed perfectly clamped in the modal while it is hard to ideally clamp them in the reality. The errors in damping ratios of the higher modes turn to be more significant. These errors could come from the Rayleigh damping. The parameters chosen here can only ensure the accuracy of damping ratios for three modes. In this case, the first three modes are chosen to determine the Rayleigh damping parameters.

Table 3.2.1 The experimental and simulation results (C-C plate with ACL)

	Mode					
	1	2	3	4	5	6
Measured natural frequency (Hz)	*54.53*	*81.50*	*157.47*	*195.59*	*220.60*	*304.02*
Calculated natural frequency (Hz)	*56.21*	*85.53*	*162.00*	*199.26*	*233.94*	*314.07*
Measured damping ratio	*0.0344*	*0.0351*	*0.0413*	*0.0366*	*0.0341*	*0.0357*
Calculated damping ratio	*0.0353*	*0.0331*	*0.0479*	*0.0402*	*0.0417*	*0.0434*

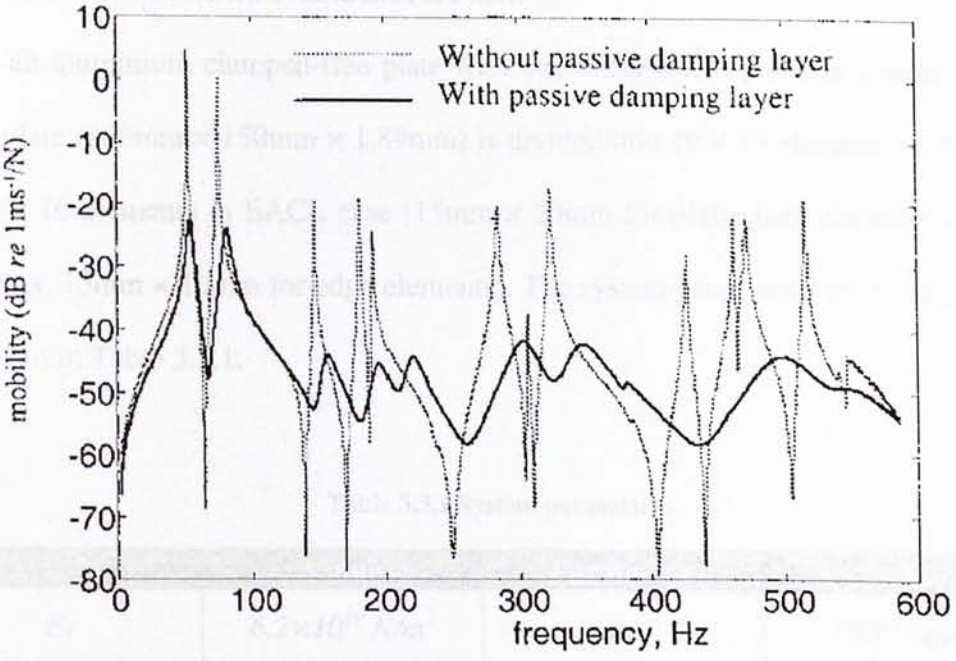

Figure 3.2.1 Experimental result of Clamped-Clamped plate with ACL treatment

(Chantalakhana and Stanway, 2000)

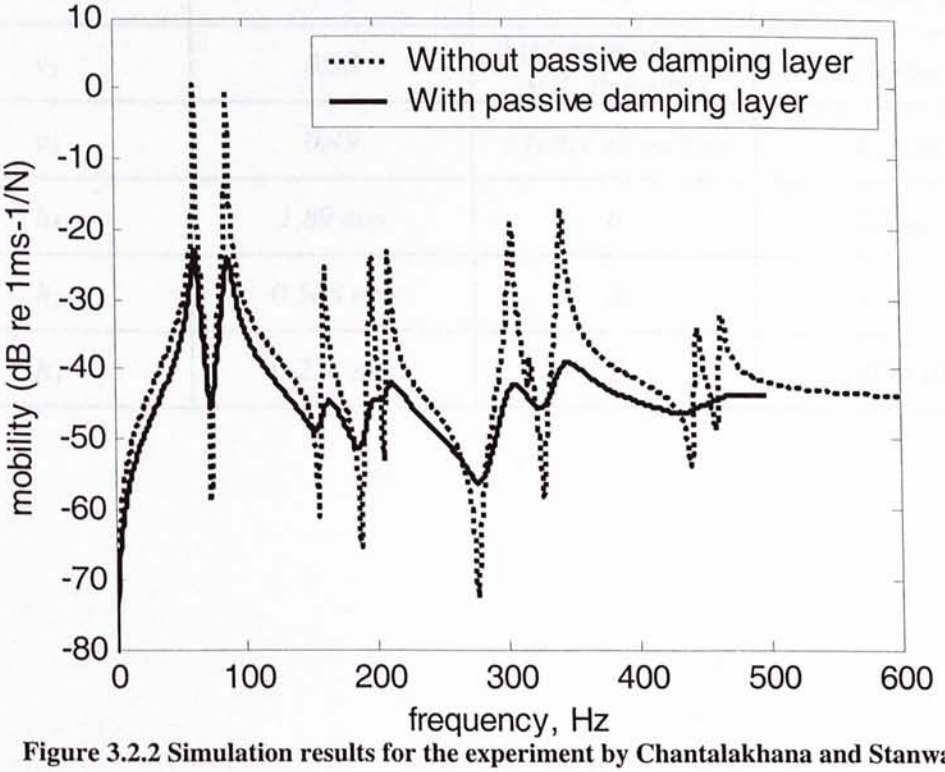

Figure 3.2.2 Simulation results for the experiment by Chantalakhana and Stanway

3.3 *Cantilever Plate with ACL/EACL Patch*

Here, an aluminium clamped-free plate with one ACL/EACL patch is considered. The plain plate (300mm × 150mm × 1.89mm) is divided into 10 × 15 elements in ACL case or 10 × 16 elements in EACL case (15mm × 20mm for plain plate elements and ACL elements, 15mm × 10mm for edge elements). The system parameters used in the models are given in Table 3.3.1.

Table 3.3.1 System parameters

	Value	Parameter	Value
E_1	6.2×10^{10} N/m^2	ρ_1	7600 kg/m^3
E_2	$2*(1+\nu_2)*G_2$ N/m^2	ρ_2	1250 kg/m^3
E_3	6.9×10^{10} N/m^2	ρ_3	2713 kg/m^3
ν_1	0.33	G_2	4.93×10^5 Pa
ν_2	0.33	*a (plane plate and ACL elements)*	20 mm
ν_3	0.49	*a (edge elements)*	10 mm
h_1	1.89 mm	*b*	7.5 mm
h_2	0.508 mm	α	0.279
h_3	0.254 mm	β	1.06×10^5

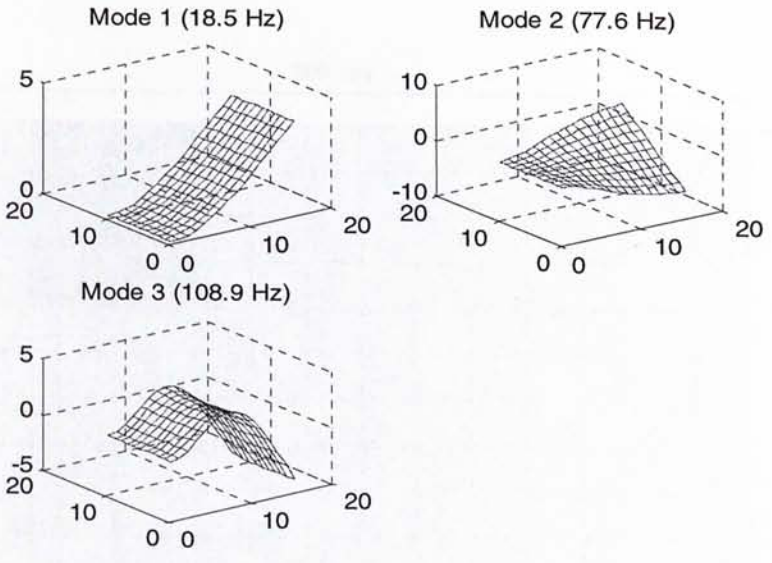

Figure 3.3.1 The first three mode shapes of the C-F plain plate

Figure 3.3.1 shows the simulation results for the first three mode shapes of the plain plate. Observing the mode shapes, we can approximately determine the location and the coverage of the ACL and EACL patches (the location optimization will be discussed in next chapter).

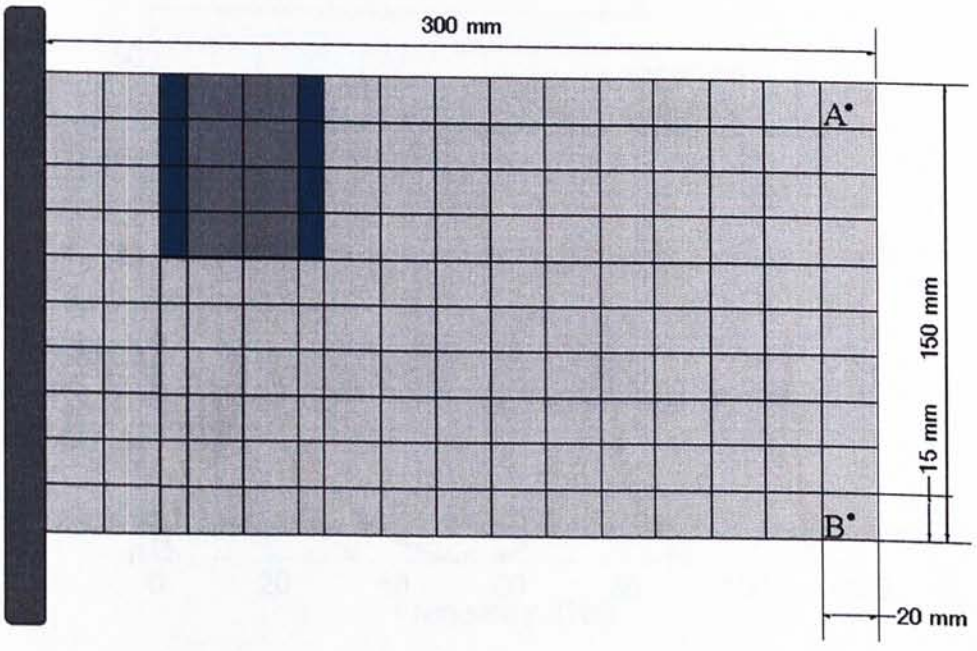

Figure 3.3.2 Finite element mesh of the C-F plate with single EACL patch

For the ACL case, the mesh of the plate consists of 10 × 15 elements and 12 of them are covered with a 60mm × 60mm ACL patch. For the EACL case, the mesh contains 10 × 16 elements as shown in Figure 3.3.2, where 16 of the elements are covered with the EACL patch.

The viscoelastic material is 3M ISD 112 with thickness of 10 mil. Three-term GHM method is used to model this VEM and the GHM parameters α_k, ξ_k and ω_k are given by Liao [1997] as Table 2.3.1. The piezoelectric constraining layer is made of PZT ceramics (Piezo System Inc., PSI-5A-S4-ENH, T120-A4E-602) with dimension 60mm × 60mm × 0.508mm.

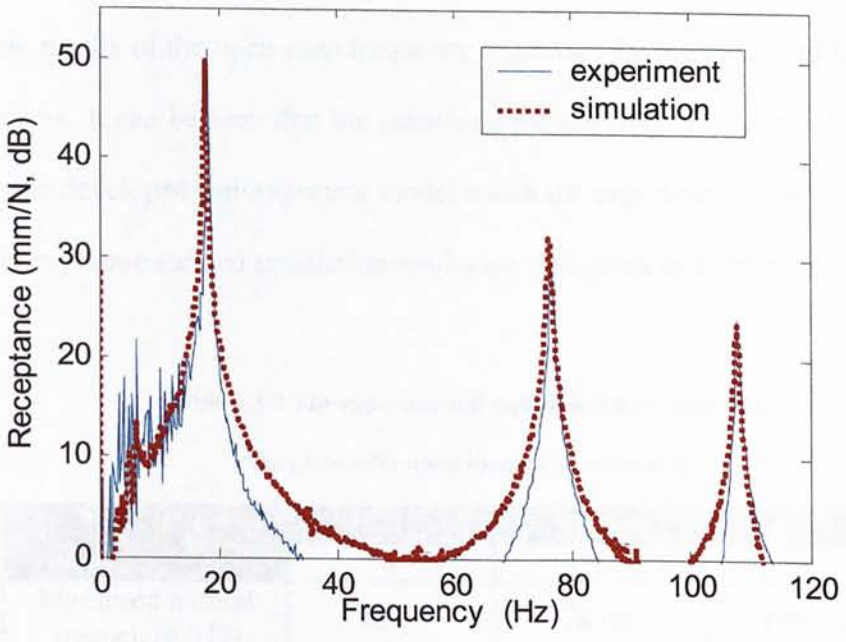

Figure 3.3.3 Open loop frequency response of the plate with ACL

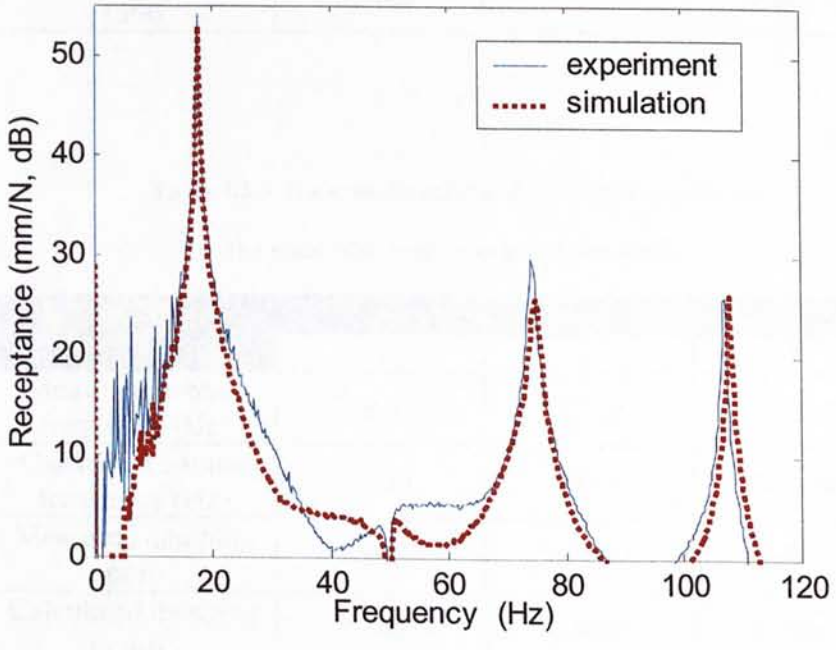

Figure 3.3.4 Open loop frequency response of the plate with EACL

Figure 3.3.3 and Figure 3.3.4 show the comparison between the experimental and simulation results of the open loop frequency responses for the ACL and EACL treated plate systems. It can be seen that the calculated natural frequencies and damping ratios by using the developed finite element model match the experimental results closely. The open loop experimental and simulation results are also given in Tables 3.3.1 and 3.3.2.

Table 3.3.2 The experimental and simulation results for the plate with open loop ACL treatment

	Mode		
	1	2	3
Measured natural frequency (Hz)	*18.00*	*76.66*	*106.58*
Calculated natural frequency (Hz)	*17.93*	*76.52*	*106.33*
Measured damping ratio	*0.0036*	*0.0042*	*0.0041*
Calculated damping ratio	*0.0037*	*0.0036*	*0.0041*

Table 3.3.3 The experimental and simulation results for the plate with open loop EACL treatment

	Mode		
	1	2	3
Measured natural frequency (Hz)	*18.37*	*77.12*	*107.91*
Calculated natural frequency (Hz)	*18.21*	*78.03*	*108.49*
Measured damping ratio	*0.0033*	*0.0031*	*0.0042*
Calculated damping ratio	*0.0035*	*0.0036*	*0.0042*

CHAPTER FOUR

STUDIES ON EACL PATCH LOCATION

In this chapter, the discussion will be focused on parametric study based on the model validated in previous chapter. There are several issues affecting the vibration of the plate with EACL patch. For example

(1) boundary conditions of the plate

(2) dimension of the plate

(3) dimension of the EACL patch

(4) location of the EACL patch

(5) material property of the VEM layer

(6) material property of the glue used as the edge element

(7) frequency of interest under external excitation

In the following numerical examples, the patch location will be studied for the passive damping ratio and actuating ability. Some optimization will be done to determine the patch location in the implementation.

4.1 Overview of the Numerical Examples

In the numerical examples, the model with the dimension described in section 3.3 will be used. As shown in Figure 4.1.1, the dimension of the rectangular base plate is 300mm × 150mm × 2mm with one side clamped. The EACL patch is 60mm × 60mm and the patch location will be varied all over the base plate in the following simulation.

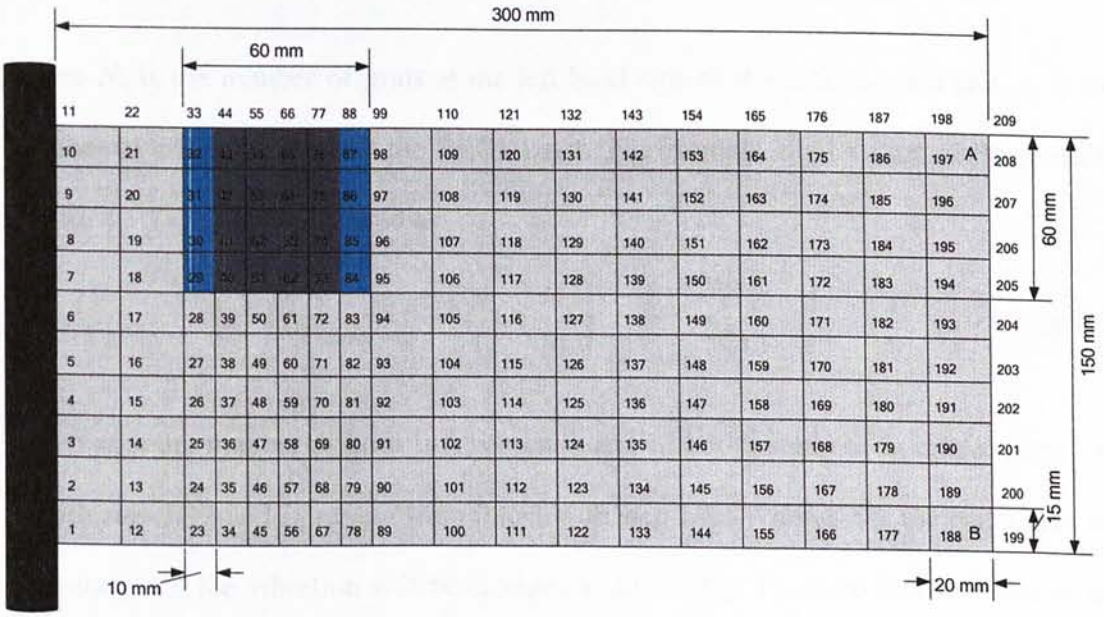

Figure 4.1.1 EACL treated plate dimension and patch location

The viscoelastic material used here is also 3M ISD 112 with thickness of 10 mil. Three-term GHM method is used to model this VEM and the GHM parameters α_k, ξ_k and ω_k are given by Liao [1997]. The piezoelectric constraining layer is made of PZT ceramics (Piezo System Inc., PSI-5A-S4-ENH) with size 60mm x 60mm. The plate is divided into 10 × 18 elements (15mm × 20mm for plain plate elements, 15mm × 10mm for edge elements and ACL elements). As we can see from Figure 4.1.1, the EACL

patch size is fixed and the patch is meshed into 4 × 6 elements where the elements with dots denote the edge elements and the hatched elements denote the ACL elements.

In order to specify the location of the EACL patch two non-dimensional parameters L_x and L_y, are defined as

$$\begin{aligned} L_x &= \frac{N_x}{12} \\ L_y &= \frac{N_y}{6} \end{aligned} \tag{4.1.1}$$

where N_x is the number of grids at the left hand side of the EACL patch and N_y is the number of grids at the top of the EACL patch. For example, the location of the patch in Figure 4.1.1 can be represented as

$$\{L_x \quad L_y\}_{figure\ 4.1.1} = \left\{\frac{N_x}{12} \quad \frac{N_y}{6}\right\}_{figure\ 4.1.1} = \left\{\frac{2}{12} \quad \frac{0}{6}\right\} = \left\{\frac{1}{6} \quad 0\right\} \tag{4.1.2}$$

The maximum number of grids is 6 vertically and 12 horizontally so L_x ranges from 0 to 1 with step 1/12 and L_y ranges from 0 to 1 with step 1/6. When L_x=0, the patch is at the boundary and the vibration will be changed significantly. To avoid this situation in the simulation, L_x varies from 1/12 to 1.

In the following sections, the plate vibration characteristics will be studied by changing these two parameters.

In the simulation, the first six vibration modes of the plate are analyzed and the first five of them are compared. Figure 4.1.2 shows the first six mode shapes. Modes 1, 3 and 5 are bending modes; modes 2, 4 and 6 are torsion modes. Those modes are decoupled in the simulation and they can be studied individually.

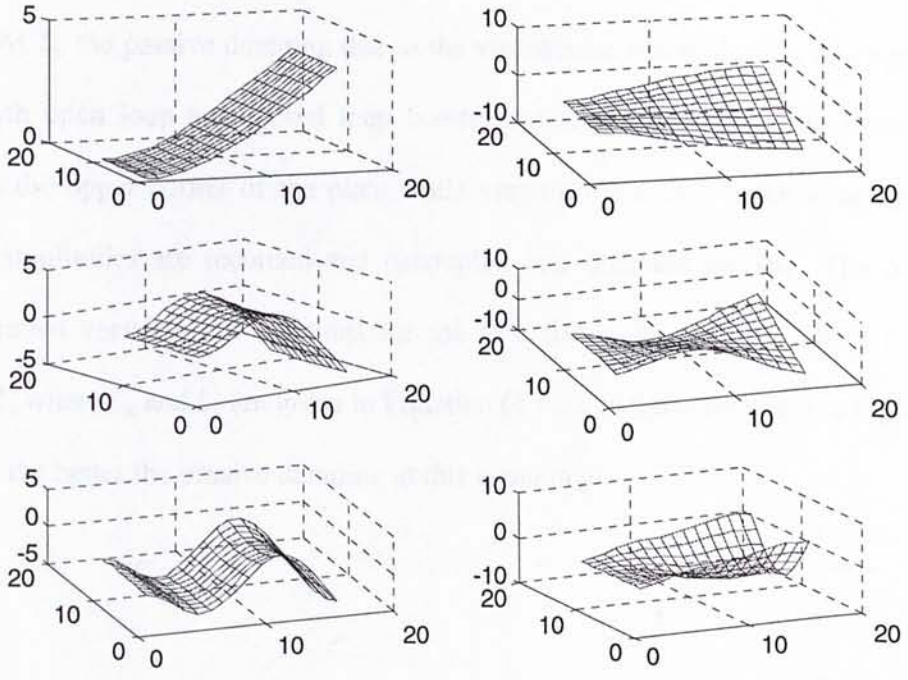

Figure 4.1.2 The first six mode shapes of the cantilever plate

4.2 *Patch Location on Passive Damping Ability*

For the EACL, the passive damping due to the viscoelastic material plays an important role in both open loop and closed loop control cases. In this section, an impulse is applied to the upper corner of the plate while varying the EACL patch location. The vibration amplitudes are recorded and decoupled into different modes. The passive damping ratios versus patch locations for the first five modes are shown in Figures 4.2.1-4.2.5, where L_x and L_y are given in Equation (4.1.2). In those figures, the higher the surface is, the better the passive damping at this location is.

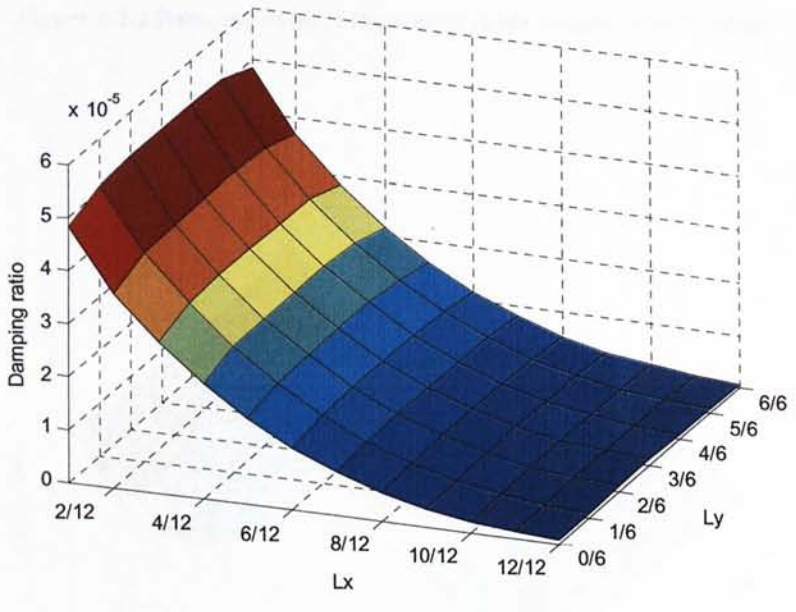

Figure 4.2.1 Damping ratio of the first mode versus patch location

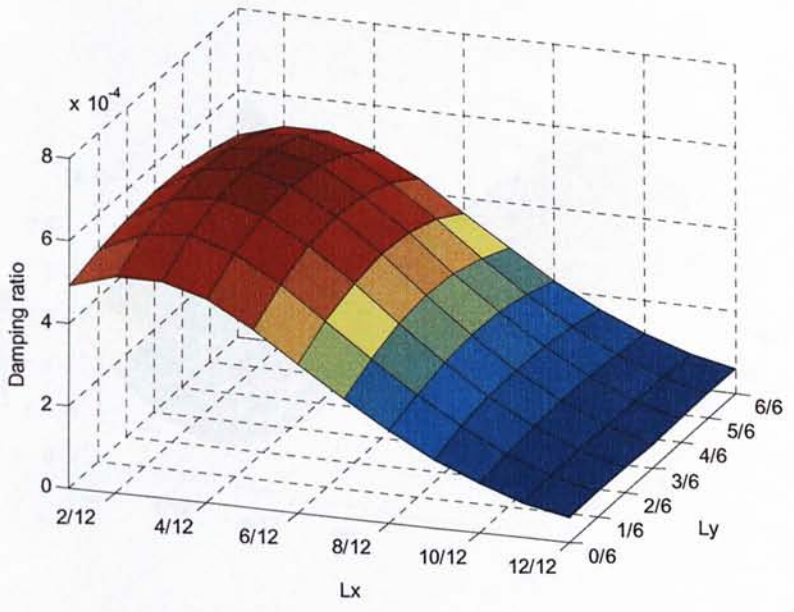

Figure 4.2.2 Damping ratio of the second mode versus patch location

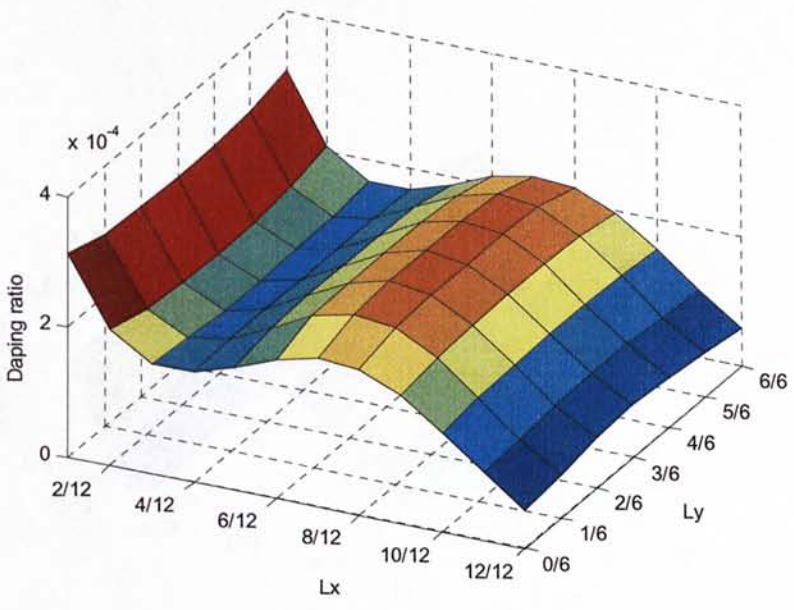

Figure 4.2.3 Damping ratio of the third mode versus patch location

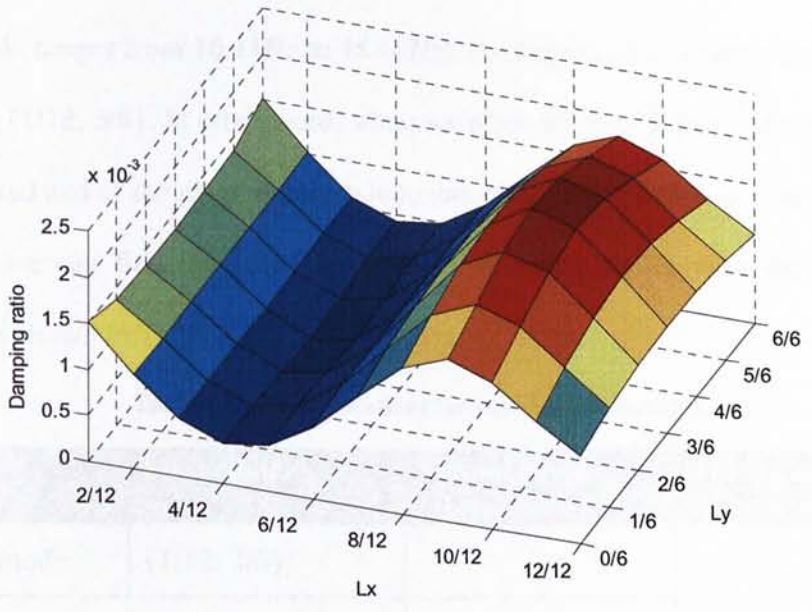

Figure 4.2.4 Damping ratio of the fourth mode versus patch location

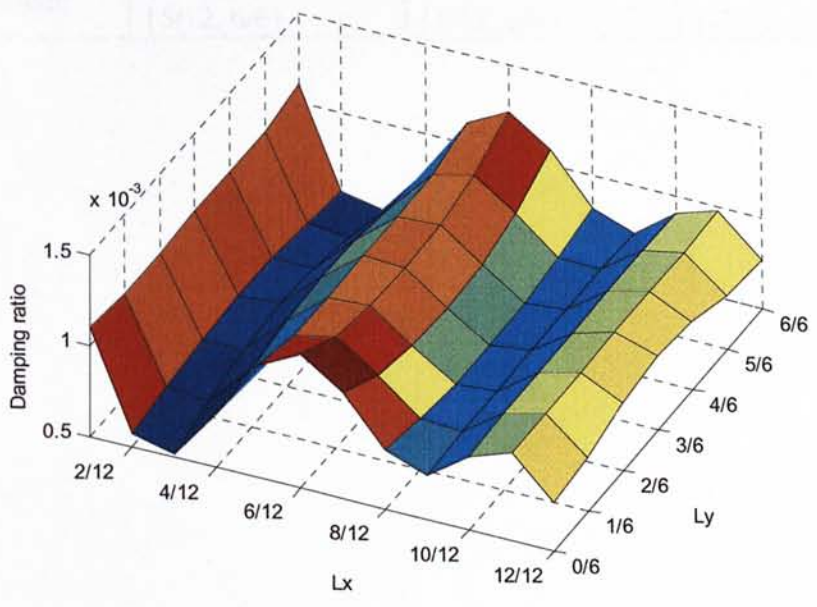

Figure 4.2.5 Damping ratio of the fifth mode versus patch location

We can see from Figure 4.2.1 that for the 1st vibration mode (natural frequency of this mode ranges from 16.11Hz to 18.60Hz), the largest passive damping ratio occurs at location {1/12, 3/6}. In other word, when we place the EACL patch at the middle line near the fixed end of the plate, the open loop damping for the first mode can be obtained. Similarly, we can find the patch location for different modes with the best passive damping as shown in Table 4.2.1.

Table 4.2.1 Patch locations for best passive damping

	First choice	Second choice (if available)	Third choice (if available)
the 1st mode	{1/12, 3/6}		
the 2nd mode	{3/12, 3/6}		
the 3rd mode	{1/12, 0/6} or {1/12, 6/6}	{7/12, 3/6}	
the 4th mode	{9/12, 3/6}	{1/12, 0/6} or {1/12, 6/6}	
the 5th mode	{6/12, 0/6} or {6/12, 6/6}	{1/12, 0/6} or {1/12, 6/6}	{11/12, 0/6} or {11/12, 6/6}

4.3 Patch Location on Actuating Ability

In the closed loop vibration system, the active damping due to the piezoelectric control force induced by voltage is of our interest. Due to the size of the FEM formulation, it will take long time to compute the closed loop damping for each mode while varying location (there are 7×13 locations for five modes; 27 minutes for each case). Therefore, instead of the closed loop damping ratio, the actuating ability is analyzed.

In Section 4.2, when the passive damping ability is tested, the plate vibration nature frequencies (the first five modes are considered) of every single patch location is computed and recorded at the same time.

Here, a sinusoidal signal is applied to the EACL patch at each location. For each mode, the plate is excited to the resonance and the vibration amplitude will reach some steady value. This value is recorded to represent the actuating authority of the EACL patch at this location, for this particular vibration mode. The actuating authority can be used to describe the control authority of the PZT based actuator patch.

The resonant amplitudes versus patch locations for the first five modes are shown in Figures 4.3.1-4.3.5. In those figures, the higher the surface is, the better the actuating ability at this location is.

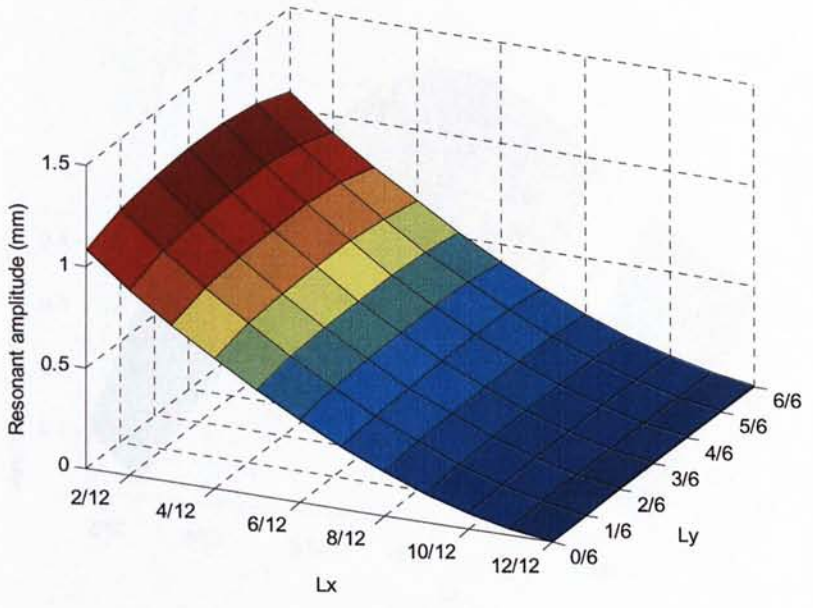

Figure 4.3.1 Resonant amplitude of the first mode versus patch location

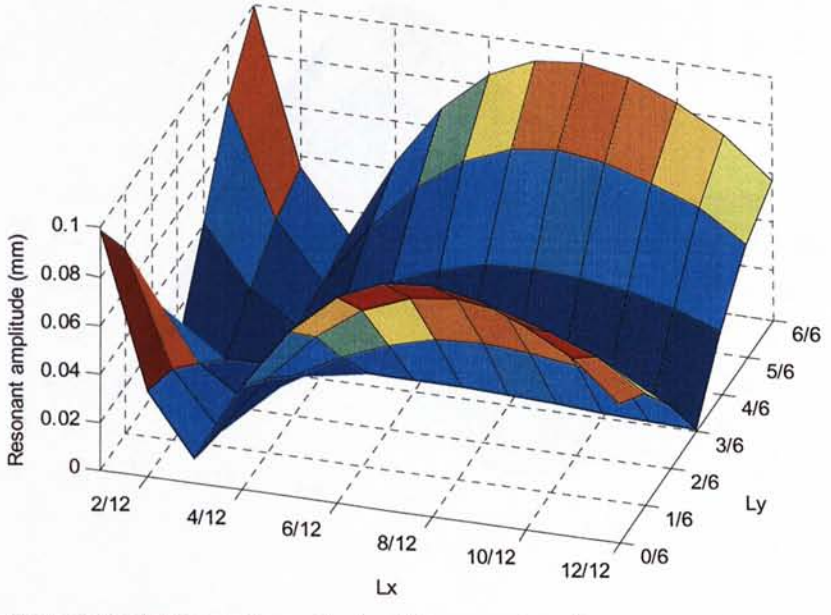

Figure 4.3.2 Resonant amplitude of the second mode versus patch location

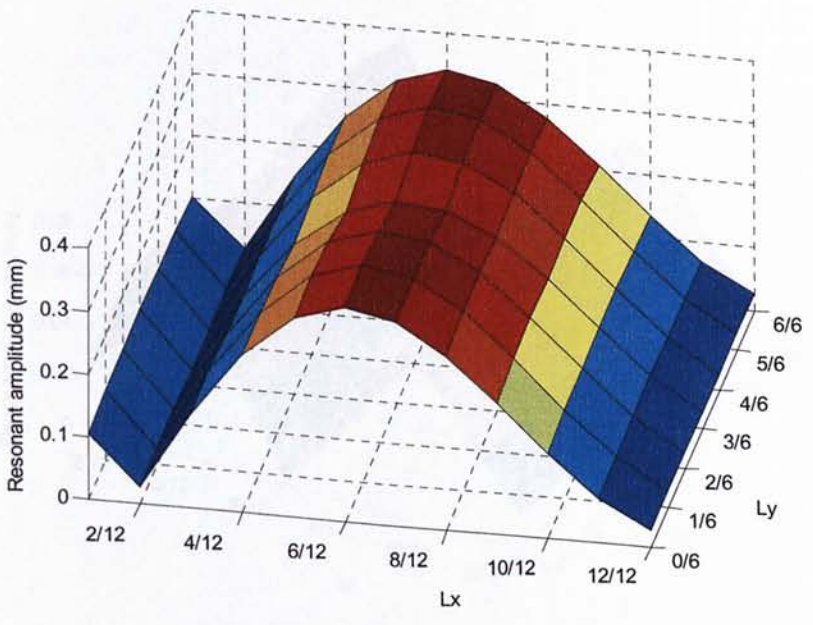

Figure 4.3.3 Resonant amplitude of the third mode versus patch location

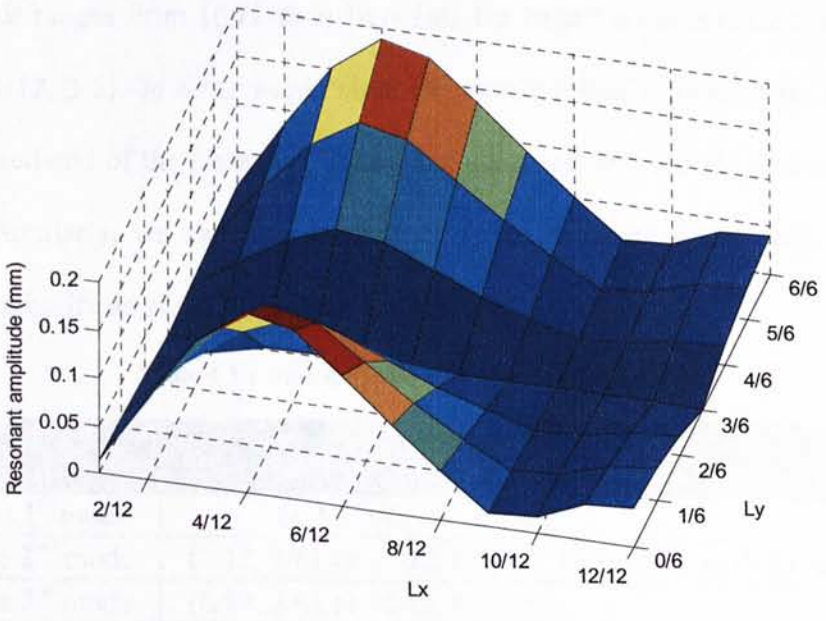

Figure 4.3.4 Resonant amplitude of the fourth mode versus patch location

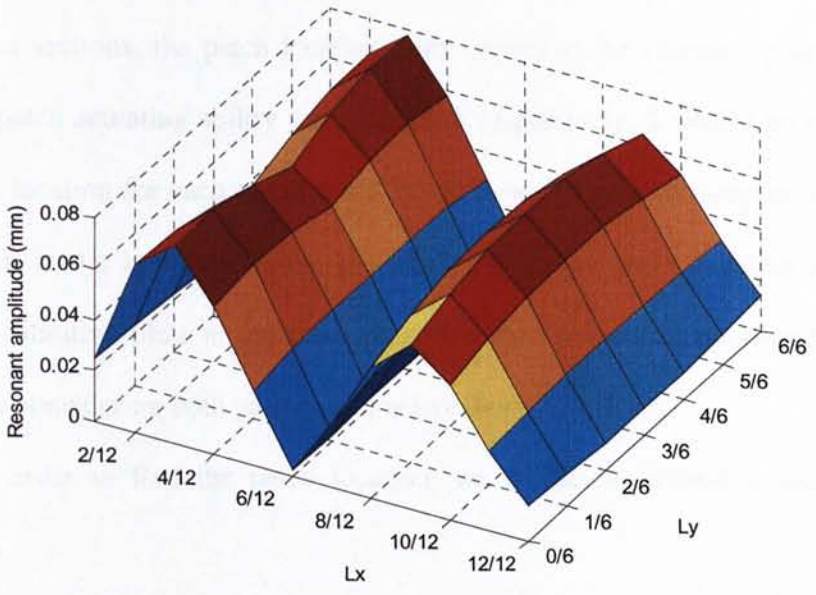

Figure 4.3.5 Resonant amplitude of the fifth mode versus patch location

We can see from Figure 4.3.1 that for the 1st vibration mode (natural frequency of this mode ranges from 16.11*Hz* to 18.60*Hz*), the largest actuating authority occurs at location {1/12, 3/6}. In other word, when we place the EACL patch at the middle line near the fixed end of the plate, the highest actuating authority for the first mode can be obtained. Similarly, we can find patch location for different modes with the highest actuating authority as given in Table 4.3.1.

Table 4.3.1 Best actuating authority patch locations

	First choice	Second choice (if available)
the 1st mode	{1/12, 3/6}	
the 2nd mode	{1/12, 0/6} or {1/12, 6/6}	{8/12, 0/6} or{8/12, 6/6}
the 3rd mode	{6/12, 2/6} or {6/12, 5/6}	
the 4th mode	{4/12, 0/6} or {4/12, 6/6}	
the 5th mode	{3/12, 2/6} or {3/12, 5/6}	{9/12, 3/6}

4.4 Discussion on Patch Location

In previous sections, the patch location with respect to the vibration passive damping ratio and patch actuating ability was discussed, respectively. It should be noted that the best patch location for each mode could be different for passive damping and actuating ability. But in the implementation, the passive damping and the active damping will affect the vibrating plate at the same time. We have to find an optimized location for each mode considering both passive and active damping effects.

In order to find the patch location, we define the hybrid damping 'location quality' as

$$Q^n(L_x, L_y) = W_p^n \zeta^n(L_x, L_y) + W_a^n A^n(L_x, L_y) \tag{4.4.1}$$

where $\{L_x, L_y\}$ is the defined patch location, Q^n is the location quality, W_p^n is the weight on the passive damping ability, W_a^n is the weight on the active damping ability, ζ^n is the damping ratio, and A^n is the steady state amplitude with superscript n denoted for the n^{th} mode.

Now the optimization problem turns to how to determine those two weights W_p^n and W_a^n. There are several aspects for the choice of W_p^n and W_a^n, for example

(1) Frequency range of interest

The active damping usually works better in low frequencies while passive damping takes effect for higher frequencies.

(2) Applied control voltage

The higher the control voltage is, the larger W_a^n is. When the control voltage is large enough, we can even ignore the passive damping effect.

(3) Desirable closed loop damping ratio

In some hybrid damping structures, the passive damping part may not provide enough damping while the passive part is fixed. Therefore, the larger the desired closed loop damping is, the larger W_a^n is.

In this research, the frequency range of interest is from 10 Hz to 120 Hz. When the average control voltage is around 30-40 volts, it is shown in Table 3.3.2 that the closed loop damping ratios of the first three modes are around 0.03 which are almost 10 times than the passive damping ratios. This is because in the partially covered EACL case, the patch is relatively small and can not provide enough passive damping for those lower modes. Therefore, W_a^n is chosen much bigger than W_p^n in this situation, we even can determine the optimized location just based on the actuating ability results (Figure 4.3.1 - Figure 4.3.3). Thus the patch location {1/12, 0/6} is chosen in the experiments discussed in next chapter. At this location, the patch has the highest actuating ability for the second mode (Figure 4.3.2), while it is near the location for providing the highest actuation for the first mode (Figure 4.3.1). It should be pointed out that location {1/12, 0/6} is not that good for the active control of the third mode (Figure 4.3.3) and that is why the third mode closed loop damping ratio is not significantly larger than the open loop damping ratio comparing with the first two modes.

CHAPTER FIVE

SYSTEM IMPLEMENTATION

In this chapter, the cantilever plate with EACL treatment discussed in previous chapters will be implemented. Positive position feedback (PPF) controller is introduced to generate the control signal for feeding to the EACL patch. This closed loop vibration system will be studied in both time domain and frequency domain. The closed loop results will be compared with the open loop system. The first three vibration modes will be observed and the control independence of the PPF controller will also be tested with this system. Moreover, the EACL treated plate will be compared with the ACL treated plate in the closed loop vibration control.

5.1 Experimental Setup

The photo of key equipment and the experimental setup is shown in Figure 5.1.1.

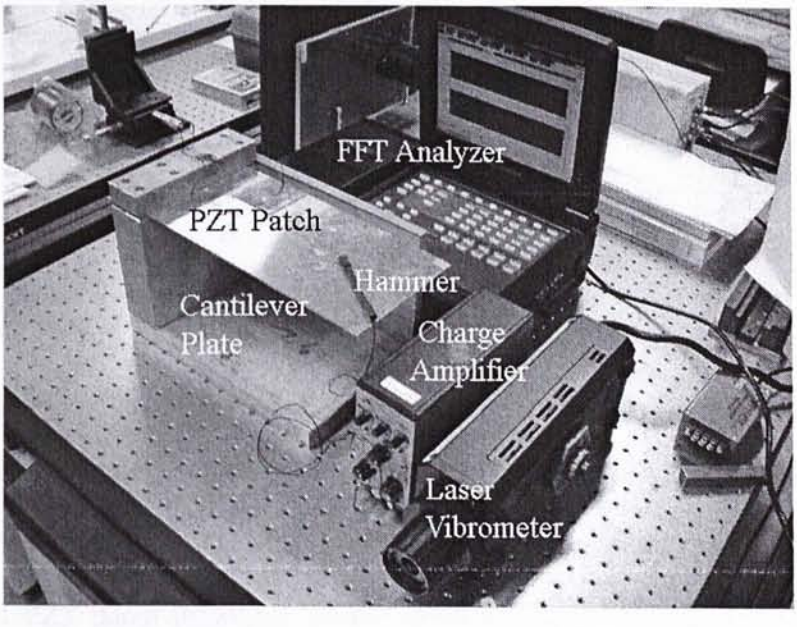

Figure 5.1.1 The cantilever plate and related equipment

5.1.1 Open loop test

In the open loop test discussed in the model validation (Chapter 4), a hammer (Brüel & Kjær 8203) is used to hit the cantilever plate near the corner of the free end (point A in Figure 3.3.2) to perform an impulse test. Both the force input from the hammer and the displacement near the corner of the plate (point B in Figure 3.3.2) from the laser vibrometer (Polytec OFV 303, 3001) are input to the FFT analyzer (ONO SOKKI CF-3400) to process the data.

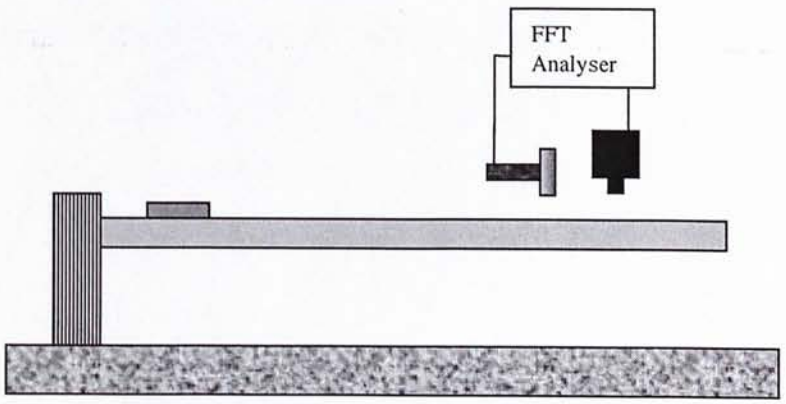

Figure 5.1.2 The open loop experimental setup

5.1.2 Closed loop test

In the closed loop test, the corner displacement signal from the laser vibrometer is fed into the PPF controller, which is implemented by a computer with a digital signal processing card (dSPACE DS1102). The PPF controller generates and feeds the control signal to the PZT patch through a power amplifier, the vibration of the plate can be controlled.

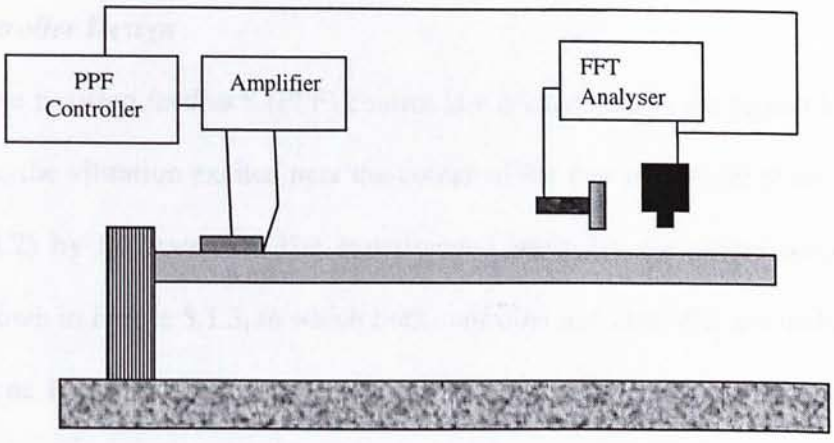

Figure 5.1.3 The closed loop experiment setup

5.2 Controller Design

The positive position feedback (PPF) control law is used here in the closed loop system to suppress the vibration excited near the corner of the free end of the plate (point A in Figure 3.3.2) by the hammer. The experimental setup for the closed loop system is already shown in Figure 5.1.3, in which both controller and amplifier are included.

Three PPF controllers are used here for the first three vibration modes (the first two bending modes and the first torsion mode as shown in Figure 4.1.2).

The PPF filter frequencies are chosen to be the same as the modal frequencies of the plate in order to obtain the best damping performance. The damping for each PPF filter is chosen based on the range of experimental data. It was pointed out by DeGuilio [2000] that damping ratio greater than 0.1 should be avoided because in some cases, greater values do not add as much damping to the plate and produce unstable controllers. The control gains are also chosen experimentally mode by mode to provide effective damping. This single EACL patch has different control authority for those three different vibration modes, thus different control gain for each PPF controller is used here. The key parameters of the controllers are given in Table 5.2.1.

It was pointed out by Han [1997] and also observed in this research that the system is unstable when the control gain is higher than some specific value. The control energy flows excessively into the high vibration modes. Three band pass filters are used for the PPF controllers and a low pass filter is used for the control output to avoid this spillover problem. This modification can also increase the control independence of different modes and suppress a specific mode of the structure while keeping other modes unaffected. The detailed control circuit is given in Figures 5.2.1 and 5.2.2.

Table 5.2.1 PPF filter parameters

	Filter Frequency (Hz)	Damping Ratio	Control Gain
1st mode	*18.5*	*0.02*	*1*
2nd mode	*77.6*	*0.01*	*0.2*
3rd mode	*108.9*	*0.03*	*0.1*

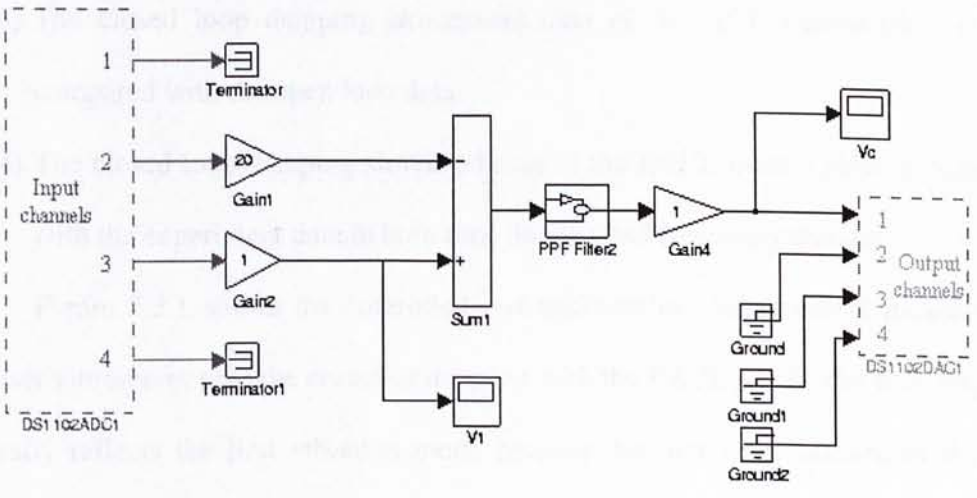

Figure 5.2.1 Overall control circuit

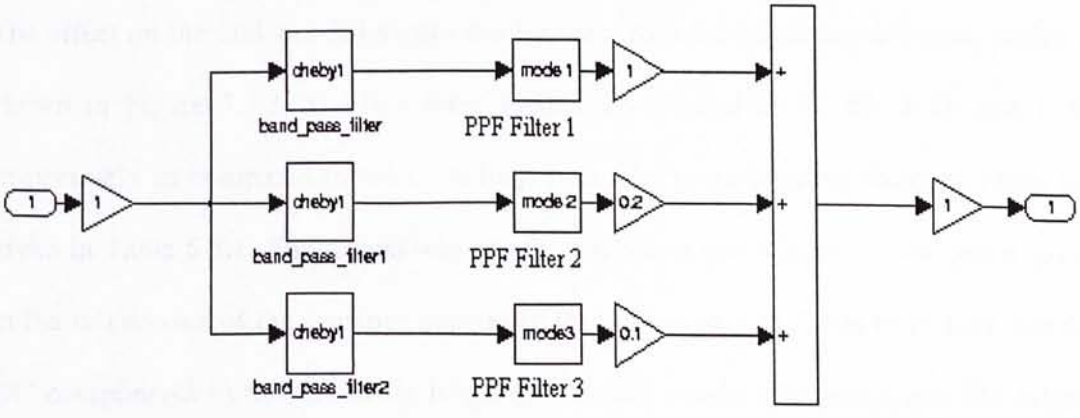

Figure 5.2.2 PPF filter

5.3 Results and Discussion

In this section, the experimental results are discussed as follows:

(1) The closed loop damping experiment data of the EACL treated plate is compared with the open loop data in both time domain and frequency domain.

(2) As PPF controller is introduced to generate the control signal, the individual mode control ability of this system is tested.

(3) The closed loop damping experiment data of the ACL treated plate is also compared with the open loop data.

(4) The closed loop damping simulated data of the EACL treated plate is compared with the experiment data in both time domain and frequency domain.

Figure 5.3.1 shows the controlled and uncontrolled displacement measured by the laser vibrometer near the corner of the plate with the EACL patch. The time response generally reflects the first vibration mode because the first mode dominates the total vibration. Compared with the open loop case, the vibration is suppressed effectively when applying the PPF control to the structure with the EACL treatment.

The effect on the 2nd and 3rd modes can be seen from the frequency response, which is shown in Figure 5.3.2. The first three modes are reduced by 10 dB, 3 dB and 1 dB respectively as compared to the open loop case. The corresponding damping ratios are given in Table 5.3.1. The reason why the third mode is not effectively damped is given in the last section of the previous chapter (refer to Section 4.4). It has to be note that the DC components in the following frequency domain results (the peaks near the origin) are brought by the rigid-body movement of the plate. Generally speaking, the vibration is well controlled by the EACL patch.

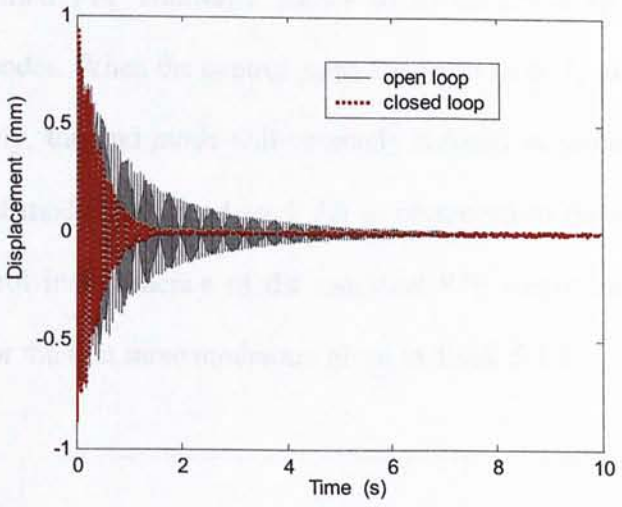

Figure 5.3.1 Time response of the EACL plate

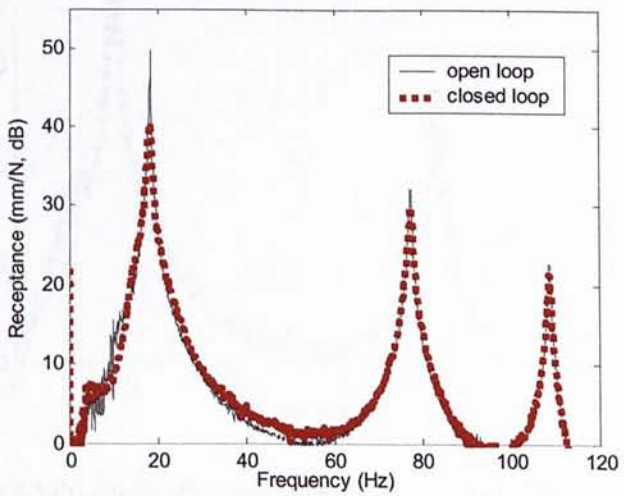

Figure 5.3.2 Frequency response of the EACL plate

Table 5.3.1 The open loop and closed loop damping ratios of EACL treated plate (first 3 modes damped)

	Mode		
	1	2	3
Open loop damping ratio	*0.0033*	*0.0031*	*0.0042*
Closed loop damping ratio	*0.0291*	*0.0110*	*0.0058*

The modified PPF controller allows us to control a specific mode without affecting other modes. When the control gains are set to be 0, 7, and 0 for the first three modes respectively, the 2nd mode will be singly reduced as shown in Figure 5.3.3, in which the second mode is reduced by 5 dB as compared to the open loop case. This verifies the control independence of the modified PPF controller. The corresponding damping ratios for the first three modes are given in Table 5.3.2

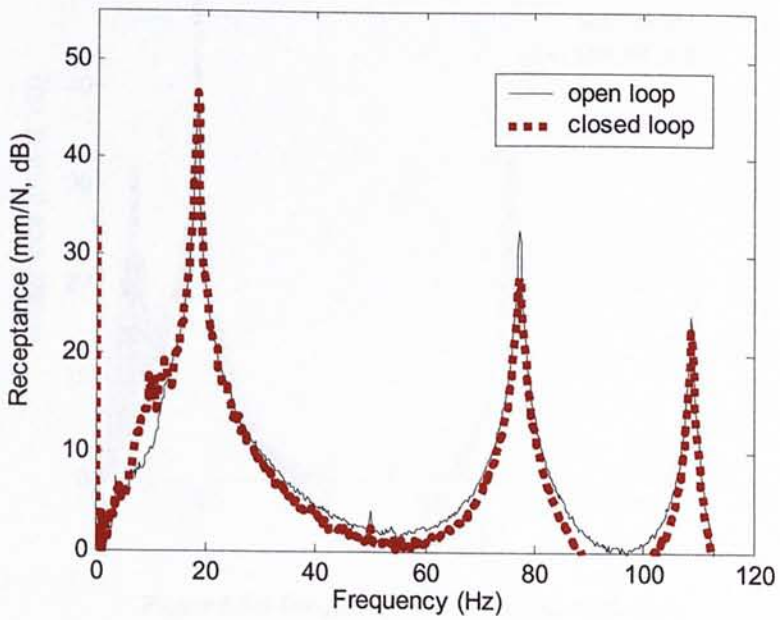

Figure 5.3.3 Frequency response of the EACL plate (2nd mode suppression)

Table 5.3.2 The open loop and closed loop damping ratios of the EACL treated plate (second mode suppressed)

	Mode		
	1	2	3
Open loop damping ratio	*0.0033*	*0.0031*	*0.0042*
Closed loop damping ratio	*0.0036*	*0.0217*	*0.0051*

When the ACL patch is bonded to the plate, it has been found that the

performance is not improved by comparing the open and closed loop frequency responses for the first three modes (see Figure 5.3.4). The average control voltage applied to the ACL patch is at the same level as that applied to the EACL patch in the experiment discussed previously (below 40 V). This brings out the effectiveness of the EACL patch with the PPF controller on the vibration control of the plate.

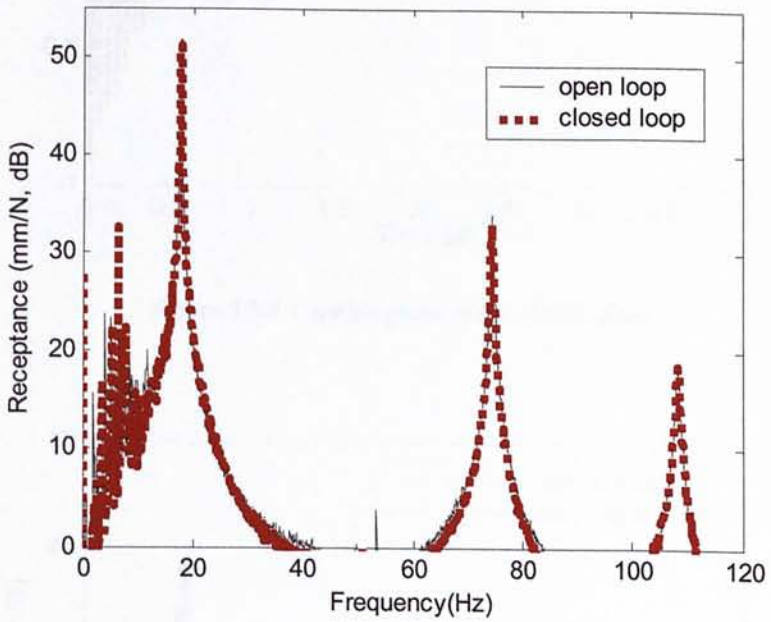

Figure 5.3.4 Frequency response of the ACL plate

The model of this closed loop system is also developed following the procedures given in previous chapters. The impulse signal recorded in the experiment is used for the simulation of an EACL treated cantilever plate with the same dimension. The time domain and frequency domain vibration responses are shown in Figure 5.3.5 and Figure 5.3.6, The accuracy of the model can be verified from the close match between the simulation and experimental results for the given frequency range.

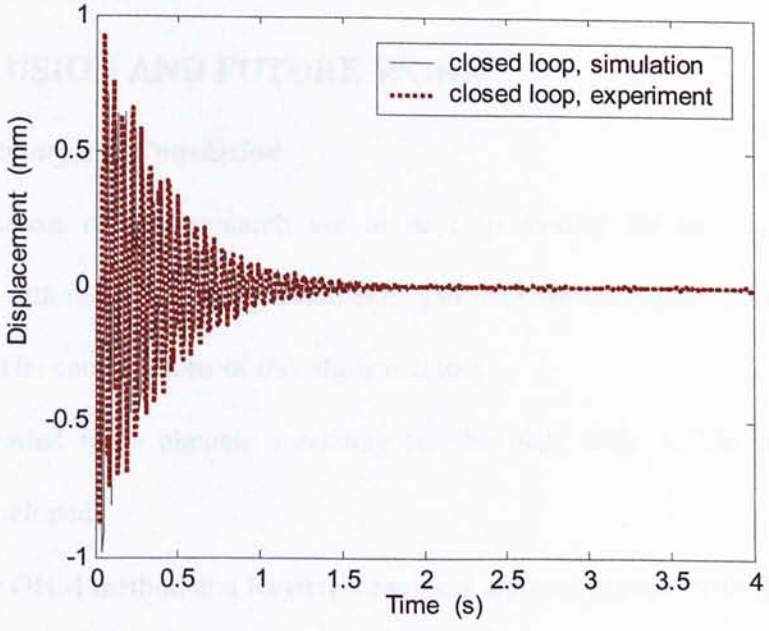

Figure 5.3.5 Time response of the EACL plate

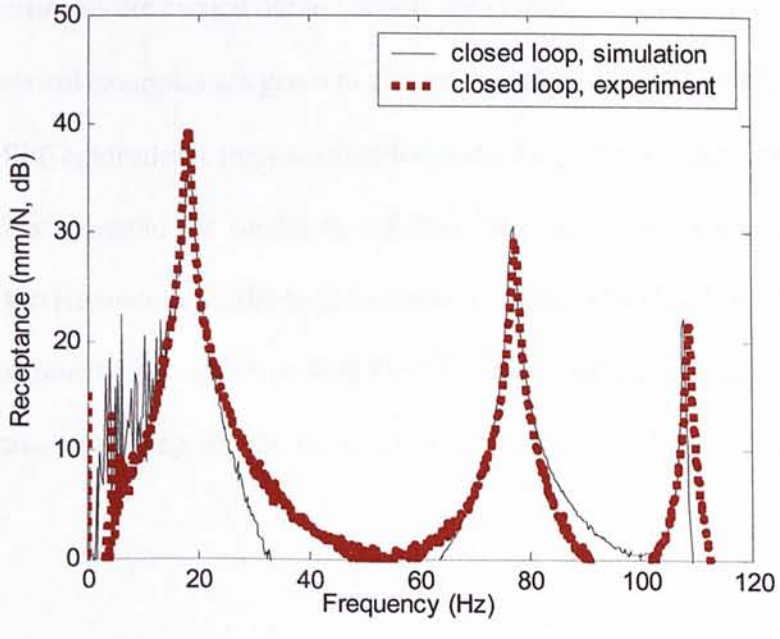

Figure 5.3.6 Frequency response of the EACL plate

CHAPTER SIX

CONCLUSION AND FUTURE WORK

6.1 Summary and Conclusion

The objectives of this research are to develop models for two dimensional plate structures with the EACL/ACL treatments, and implement the EACL treatment on plate structure. The contributions of this study include:

- detailed finite element modeling for the plate with ACL/EACL treatment is developed;
- the GHM method and Rayleigh damping are incorporated with the finite element model;
- both bending and torsion modes are considered in vibration analysis;
- experiments are carried out to validate the models;
- numerical examples are given to discuss the effect of EACL patch location;
- the PPF controller is implemented for controlling the vibration of the plate

In this research, the model is validated and the accuracy has been shown by comparing the simulation results to the experiment data. The EACL treatment has been proved to be much more effective than the ACL treatment for providing active-passive hybrid vibration damping for the plate. Thus the objectives of this research have been achieved.

6.2 Recommendations for Future Research

There are several issues worth further study on two dimensional plate structures with EACL treatments. The parametric studies on the EACL treated plates should be valuable. The size, shape and location of the EACL patch should be investigated. The edge elements considered in this research are simply located at both sides of the patch; the shape and orientation of the edge elements on the patch should be explored. The validated finite element model provides an accurate and convenient platform to study the characteristics of the plates with ACL/EACL treatments. Finally, the Matlab programs developed in this research could be rewritten with a more efficient computer language. The computing speed and the user interface need to be improved.

APPENDIX – PZT data sheet from PIEZO SYSTEMS, INC.

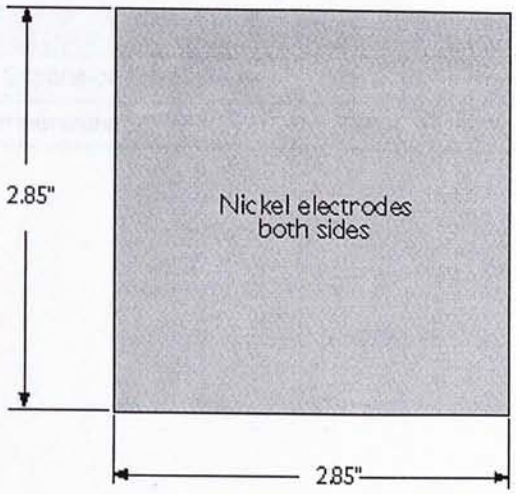

Large A4 Single Sheets

Part Number	Thickness		Capacitance
	mm	in	nF (±10%)

PIEZOELECTRIC			
Composition		Lead Zirconate Titanate	
Material Designation		Type 5A4E (Industry Type 5A, Navy Type II)	
Relative Dielectric Constant (@ 1 KHz)	K^T_3	1800	
Piezoelectric Strain Coefficient	d_{33}	390×10^{-12}	meters/Volt
	d_{31}	-190×10^{-12}	meters/Volt
Piezoelectric Voltage Coefficient	g_{33}	24.0×10^{-3}	Volt meters/Newton
	g_{31}	-11.6×10^{-3}	Volt meters/Newton
Coupling Coefficient	k_{33}	0.72	
	k_{31}	0.32	
Polarization Field	Ep	2×10^6	Volts/meter
Initial Depolarization Field	Ec	5×10^5	Volts/meter
MECHANICAL			
Density		7800	$Kg/meter^3$

Mechanical Q		80	
Elastic Modulus	Y^E_3	5.2×10^{10}	Newtons/meter^2
	Y^E_1	6.6×10^{10}	Newtons/meter^2
Poisson's Ratio	V	~.31	
THERMAL			
Thermal Expansion Coefficient		$\sim 4 \times 10^{-6}$	meters/meter °C
Curie Temperature		350	°C

BIBLIOGRAPHY

Bickford W.B., 1994, *A first course in the finite element method*, Second edition, IRWIN Press

Chantalakhana C. and Stanway R., 2000, "Active constrained layer damping of plate vibrations: a numerical and experimental study of modal controllers", *Smart Materials and Structures*, **9**, 940-952

DeGuilio A.P., 2000, *A comprehensive experimental evaluation of actively controlled piezoceramics with positive position feedback for structural damping*, Master Thesis, Virginia Tech

Ewins D.J., 1984, *Modal testing: theory and practice*, Research Studies Press

Golla D.F. and Hughes P.C., 1985, "Modeling dynamics of viscoelastic structures – a time-domain, finite element formulation", *Journal of Applied Mechanics*, **52**, 897-906

Han J.H., Rew K.H. and Lee I., 1997, "An experimental study of active vibration control of composite structures with a piezo-ceramic actuator and a piezo-film sensor", *Smart Materials and Structures*, **6**, 549-558

Kwon Y.W. and Bang H., 1997, *The finite element method using MATLAB*, CRC Press

Lam M.J. and Saunders W.R., 1995, "Modeling active constrained layer damping using Golla-Hughes-McTavish approach", *Proceedings of SPIE's Annual International Symposium on Smart Structures and Materials*, 2445, 86-97

Liao W.H. and Wang K.W., 1996, "A new active constrained layer configuration with enhanced boundary actions", *Smart Materials and Structures*, **5**, 638-648

Liao W.H., 1997, *Active-passive hybrid structural control: an enhanced active constrained cayer damping treatment with edge elements*, PhD Thesis, The Pennsylvania State University

Liao W.H. and Wang K.W. 1997, "On the active-passive hybrid control actions of structures with active constrained layer treatments", *Journal of Vibration and Acoustics*, **119(4)**, 563-572

Liao W.H. and Wang K.W., 1997, "On the analysis of viscoelastic materials for Active constrained layer damping treatments", *Journal of Sound and Vibration*, **207(3)**, 319-334

Lim Y.H., Varadan V.V. and Varadan V.K., 2002, "Closed loop finite-element modeling of active constrained layer damping in the time domain analysis", *Smart Materials and Structures*, **9**, 89-97

Liu Y. and Wang K.W., 1999, "A non-dimensional parametric study of enhanced active

constrained layer damping treatments", *Journal of Sound and Vibration*, **223(4)**, 611-644

Liu Y. and Wang K.W., 2002, "Enhanced active constrained layer damping treatment for broadband vibration suppression", *Journal of Vibration and Control*, **8**, 777-803

McTavish D.J. and Hughes P.C., 1993, "Modeling of linear viscoelastic space structures", *Journal of Vibration and Acoustics*, **115**, 103-110

Petyt M., 1990, *Introduction to finite element vibration analysis*, Cambridge University Press

Rao S.S., 1995, *Mechanical vibrations*, Addison-Wesley Publishing Company

Ro J. and Baz A., 1999, "Vibration control of plates using self-sensing active constrained layer damping", *Proceedings of SPIE's Annual International Symposium on Smart Structures and Materials*, **3672**, 200-209

Shen I.Y., 1994, "Bending-vibration control of composite and isotropic plates through intelligent constrained-layer treatments", *Smart Materials and Structures,* **3**, 59-70

Wang G. and Wereley N.M., 1999, "Piezo-actuation of sandwich plates with viscoelastic cores", *Proceedings of SPIE's 6th Annual International Symposium on Smart Structures and Materials*, **3672**, 210-225

Wang G., 2001, *Analyses of sandwich beams and plates with viscoelastic cores*, PhD Thesis, University of Maryland

Wong K.M., 2001, *Implementation and modeling of beam structures with self-sensing piezoelectric actuators*, MPhil Thesis, The Chinese University of Hong Kong